

NIST GCR 12-964

**Reducing Flammability of Polymers by
Enhancing Char Formation. Final Report.**

NIST GCR 12-964

**Reducing Flammability of Polymers by
Enhancing Char formation. Final Report.**

Takashi Kashiwagi
*Department of Fire Protection Engineering
University of Maryland
College Park, MD 20742*

Grant 60NANB9H9184

March 2012



U.S. Department of Commerce
John E. Bryson, Secretary

National Institute of Standards and Technology
Patrick D. Gallagher, Under Secretary of Commerce for Standards and Technology and Director

Notice

This report was prepared for the Engineering Laboratory of the National Institute of Standards and Technology under Grant number 60NANB9H9184. The statement and conclusions contained in this report are those of the authors and do not necessarily reflect the views of the National Institute of Standards and Technology or the Engineering Laboratory.

Reducing Flammability of Polymers by enhancing Char Formation

Final Report

60NANB9H9184

July 2011

Takashi Kashiwagi

Department of Fire Protection Engineering, University of Maryland

Table of Contents

| | |
|---|----|
| Summary..... | 1 |
| Paper “Effects of montmorillonite dispersion on flammability properties of poly(styrene-co-acrylonitrile) nanocomposites” <i>Polymer</i> , 52 , 3092-3103, 2011..... | 2 |
| Paper “Flame retardancy of poly(styrene-co-acrylonitrile) by the synergistic interaction between clay and phosphomolybdate hydrates” <i>Polymer Degradation and Stability</i> , 96 , 1000-10008, 2011..... | 14 |
| Paper “Effect of heat treatment on the morphology and properties of poly(styrene-co-acrylonitrile) / montmorillonite nanocomposites” (previously unpublished)..... | 23 |

Summary

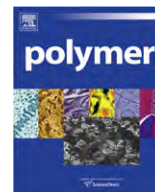
This project was started from September 1, 2009 and is ending on August 31, 2011 with a total budget of \$74,129.

One weak aspect of synthetic polymer materials compared with steel and other metals is that these materials are combustible under certain conditions. Thus, the majority of polymer-containing end products must pass some type of regulatory test to assure public safety from fire. Although halogenated flame retardants are highly effective for reducing heat release rates of commodity polymers, the future use of some of these retardants is becoming highly questionable in Europe and possibly worldwide. Therefore, new, highly effective flame retardants are urgently needed as a possible alternative to conventional halogenated flame retardants. The main objective of this research is to apply combined effects of a catalyst in a clay-based polymer nanocomposite to enhance formation of char from a resin to form a protective layer consisting of char enhanced clay network during burning.

The first study is to determine the effects of dispersion level of clay particles in poly(styrene-co-acrylonitrile), SAN on flammability properties of SAN. SAN/Cloisite 20A(95/5) nanocomposites, having five different spatial dispersion levels of the clay, were prepared by the solvent coagulation method. X-ray diffraction, transmission electron microscopy, and laser scanning confocal microscopy were used to characterize the structure and morphology of the nanocomposites. The results show that higher the spatial dispersion level of the clay reduces mass loss rate (heat release rate) of the polymer nanocomposite. The nanocomposite having highest dispersion level used in this study reduced about 60 % of the peak mass loss rate of SAN30. The results were published in *Polymer*. The paper is included in this report.

Four different catalysts, ammonium phosphomolybdate hydrate (NHPMo), melamine phosphomolybdate hydrate (MEPMo), zinc phosphomolybdate hydrate (ZnPMo), and sodium phosphomolybdate hydrate (NaPMo), were used as catalysts to enhance char in SAN40/Cloisite 20A(95/5). The only combination of the clay with NHPMo showed synergistic enhancement in promoting char formation and reducing the peak mass loss rate of SAN40. High temperature rheological data indicate the formation of a stronger network structure in SAN40/Cloisite 20A/NHPMo(92/5/3); this benefits flame retardancy by allowing fewer cracks to form in the char layer. The more continuous char layer suppresses bubble transport of degradation products as fuel vapors and the char layer acts as a heat shield, thereby reducing the mass loss rate. The results were published in *Polymer Degradation and Stability*. The paper is included in this report.

The effects of aging on flammability properties of polymer clay nanocomposites were studied by heating SAN30/Clay (95/5) nanocomposites at 80 °C for 72 hours duration. Preliminary results show that the dispersion of Cloisite 20 A in SAN30 gets worse and mass loss rate increased about 24 % by the heating. However, the heating did not affect significantly with SAN30/Cloisite 30B (95/5). It appears that affinity between the resin and clay tends to affect the level of aging. Further study is needed to confirm this trend.



Effect of montmorillonite dispersion on flammability properties of poly(styrene-co-acrylonitrile) nanocomposites[☆]

Meifang Liu^{a,b,*}, Xin Zhang^c, Mauro Zammarano^a, Jeffrey W. Gilman^a, Rick D. Davis^a, Takashi Kashiwagi^{a,*}

^aFire Research Division, National Institute of Standards and Technology, Gaithersburg, MD 20899-8665, United States

^bThe State Key Laboratory of Polymer Materials Engineering, Polymer Research Institute of Sichuan University, Chengdu 610065, China

^cDepartment of Materials Science, University of Maryland, College Park, MD 20742, United States

ARTICLE INFO

Article history:

Received 24 February 2011

Received in revised form

28 April 2011

Accepted 1 May 2011

Available online 7 May 2011

Keywords:

Dispersion

Flammability

Montmorillonite

ABSTRACT

Poly(styrene-co-acrylonitrile)/Cloisite 20A (95/5) nanocomposites, having various spatial dispersion levels of the clay, were prepared with controlling clay concentrations in a solvent by the coagulation method. X-ray diffraction, transmission electron microscopy and laser scanning confocal microscopy were used to characterize the structure and morphology of the nanocomposites on a nano-scale and on a micro-scale. Quantitative analysis of clay spatial dispersion in the nanocomposites based on the laser scanning confocal microscopy images was conducted from three different perspectives: 1) clay spatial distribution; 2) the non-clay-occupied domain size; and 3) the relationship between the frequency and intensity of pixels in the images. The results from these quantitative methods indicate that nanocomposites with different spatial dispersion levels of clay in the poly(styrene-co-acrylonitrile) matrix were obtained. Evidently, the Δd_{001} data from the X-ray diffraction was found to be not useful in measuring the clay dispersion in the nanocomposites. The effect of clay dispersion on the flammability properties of the nanocomposites and relevant mechanism of the clay dispersion having influence on flammability were also investigated. In radiant gasification experiments at 50 kW/m², the best clay dispersion yielded a 32% reduction in peak mass loss rate, as compared to the nanocomposites with the worst dispersion.

© 2011 Elsevier Ltd. All rights reserved.

1. Introduction

Over the past two decades, there has been a significantly increasing interest in polymer/montmorillonite (MMT) nanocomposites [1–4]. It is well established that the dispersion of MMT clay is a key factor to obtain good physical properties of the nanocomposites, but the qualitative relationship between the clay dispersion and other properties, especially flammability properties, of the nanocomposites has not been well established [5–13]. As early as the year 2000, Gilman et al. prepared polystyrene/montmorillonite (PS/MMT) nanocomposites by varying the organic modifiers in the clay [5]. Intercalated and exfoliated structures of PS/MMT nanocomposites were characterized by transmission electron

microscopy (TEM). They found that the nanodispersion had an influence on the flammability. In 2001, Wilkie et al. reported that PS/MMT nanocomposites with an intercalated structure gave a lower peak heat rate compared with the exfoliated structure [6]. They controlled the morphology of the nanocomposites by selecting a proper organic modifier. In 2005, Stretz et al. prepared poly(styrene-co-acrylonitrile) (SAN) nanocomposites with different organo-modified clays and found that the clay dispersion, characterized by X-ray diffraction (XRD) and TEM, had an insignificant effect on the flammability [7]. In 2008, Bourbigot et al. assessed the clay dispersion by TEM and solid state nuclear magnetic resonance (NMR), and also demonstrated that the clay dispersion did not affect the flammability for polyamide 6 (PA6)/MMT nanocomposites with different organo-modified clays [9].

These different conclusions about the effect of clay dispersion on the flammability are potentially due to variations in the organic modifiers and characterization methods used for the spatial dispersion of clay. Firstly of all, all the samples with different MMT dispersion in these studies were prepared with varying organic modifiers in the clay. It has been reported that the organic modifiers also affect the properties of polymer nanocomposites

[☆] This study was carried out by the National Institute of Standards and Technology (NIST), an agency of the US Government which, by statute, is not subject to copyright in the US.

* Corresponding authors. Fire Research Division, National Institute of Standards and Technology, Gaithersburg, MD 20899-8665, United States

E-mail addresses: liumf2009@gmail.com (M. Liu), takashi.kashiwagi@nist.gov (T. Kashiwagi).

[10,14–18]. Additionally, the true loading of MMT in the samples is not the same due to the different amounts of organic modifier when the organoclay loading is kept at the same concentration in the nanocomposites. Moreover, XRD combined with TEM is the most commonly used method to determine the structure and morphology of nanocomposites [1,19]. However, we find that the Δd_{001} (shift in d_{001} interlayer spacing from pristine clay to the clay in composites) is not be a good quantitative index of the clay spatial dispersion, especially for different clay since different clay have different d_{001} . For some clays (Cloisite 15 A), the d_{001} of polymer/MMT composites is around the same as that of clay itself but the nano-structure was confirmed by TEM [20,21]. TEM provides a more direct observation of the changes of clay layers in clay stacks as well as the homogeneity of clay dispersion in the polymer matrix, but TEM images are representative of only an extremely small volume in the sample. Lastly, most previous works has presented qualitative descriptions of spatial dispersion instead of quantitative ones, excepting Bourbigot's work [9].

The objective of this study is to quantitatively measure the spatial dispersion level of clay in SAN30 nanocomposites and to determine the effect of this parameter on the flammability properties of the nanocomposites. SAN/MMT nanocomposites with the same organoclay source and the same loading were prepared by the coagulation method, which excludes the effects of different organic modifiers and MMT loading on the flammability [22]. The dispersion of the clay in the nanocomposites can be controlled by varying the clay concentration in a solvent. Additionally, laser scanning confocal microscopy (LSCM), which has proved to be an effective method to obtain the spatial dispersion level of particles on a micro-scale in polymer nanocomposites in previous studies [23,24], can fill up the deficiencies of XRD and TEM. Therefore, LSCM combined with XRD and TEM, used in this paper can sufficiently measure the spatial dispersion level of the clay in the SAN30/MMT nanocomposites. Mechanisms of how the clay dispersion level impacts the flammability properties of SAN30/MMT nanocomposites are also discussed.

2. Experimental section

2.1. Materials

SAN30 (The mass fraction of acrylonitrile in the resin is 30%) was purchased from Aldrich¹. The organoclay (Cloisite 20A) with dimethyl, dehydrogenated tallow, quaternary ammonium chloride surfactant, was provided by Southern Clay Products, Inc. Tetrahydrofuran (THF) was purchased from Fisher Scientific.

2.2. Preparation of samples

SAN30/20A nanocomposites with a mass fraction of 5% Cloisite 20A were prepared by the coagulation method [22]. 23.75 g SAN30 was dissolved in 100 ml THF while 1.25 g Cloisite 20A was added in 150 ml THF and then the 20A/THF mixture was sonicated for 1 h (sonicator: Branson 2210). Then, the sonicated THF mixture was added to the stirred THF with SAN30; this mixture (5.0 mg/ml clay concentration in THF) was bath sonicated for 1 h and then stirred for 20 h. The concentration of Cloisite 20A in the THF mixture was varied (1.0 mg/ml, 2.0 mg/ml, 5.0 mg/ml, 7.5 mg/ml and 10.0 mg/ml) to control the extent of clay dispersion in SAN30. The suspension was then precipitated into a large amount of distilled

water ($V_{\text{THF}}/V_{\text{water}} \approx 1/8$) to remove the solvent. The suspension was filtered while washing with distilled water and then the polymer–clay mixture was put into an aluminum foil pan for drying in a chemical hood overnight. Then, it was placed in a vacuum oven at 100 °C under the vacuum for 24 h. The dried samples were ground and then dried in a vacuum oven again to remove the remaining solvent. Then, the SAN30/20A powder were compression molded using a Carver press between 170 °C and 180 °C for 15 min to make samples for XRD, TEM, LSCM and rheological tests (discs of 25.0 mm \pm 0.5 mm in diameter and 1.0 mm \pm 0.1 mm thickness) and samples for measuring flammability properties (discs of 75.0 mm \pm 0.5 mm in diameter and 4.0 mm \pm 0.1 mm thickness).

2.3. Characterization

2.3.1. Morphological characterization of SAN30/20A composites

XRD data were obtained using a Bruker D8 Advance with a Cu K α tube and 12 mm variable slit at a step size of 0.01665° and time step of 0.75 s. The uncertainty of the d-spacing was 0.5 Å (2σ) as determined by running Cloisite 20A three times.

TEM was conducted with a JEOL JEM 2100F TEM working at 200 kV with a Gatan CCD camera at 200 keV. The TEM sample was prepared with a Leica UC-6 ultramicrotome with a Diatome diamond knife at room temperature. The thickness of sections was thinner than 100 nm.

The morphologies of the clay in the samples were also evaluated using an LSCM (Model LSM510, Carl Zeiss Inc.). The confocal microscope utilizes coherent laser light and collects reflected light exclusively from a single plane. A laser (405 nm) was used as the coherent light and images were taken at (100 \times) magnification with an Epiplan-Neofluar (100 \times)/1.30 oil-pool objective. About one hundred and twenty two-dimensional (2D) images (optical slices with 1024 pixels \times 1024 pixels), with scan size 84.2 μm \times 84.2 μm , were taken in steps of 100 nm. Rough surface images were excluded, and the 2D projection images and 3D images were constructed from one hundred 2D images by LSCM software.

In previous paper [24], the standard χ^2 statistic and the relative dispersion index were proved to be effective for characterizing the quantitative dispersion of carbon nanotubes in a polymer. Since the two methodologies are similar and the χ^2 test (Chi-square test/Chi-square goodness-of-fit test) is one of the most widely used in

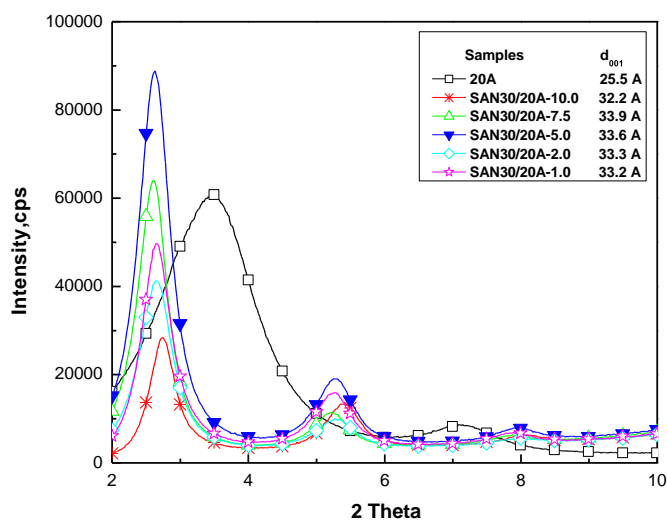


Fig. 1. XRD curves of 20A and SAN30/20A (95/5) composites prepared from different clay concentrations in THF (10.0 mg/ml, 7.5 mg/ml, 5.0 mg/ml, 2.0 mg/ml and 1.0 mg/ml).

¹ Certain commercial equipments, instruments, materials, services or companies are identified in this paper in order to specify adequately the experimental procedure. This in no way implies endorsement or recommendation by NIST.

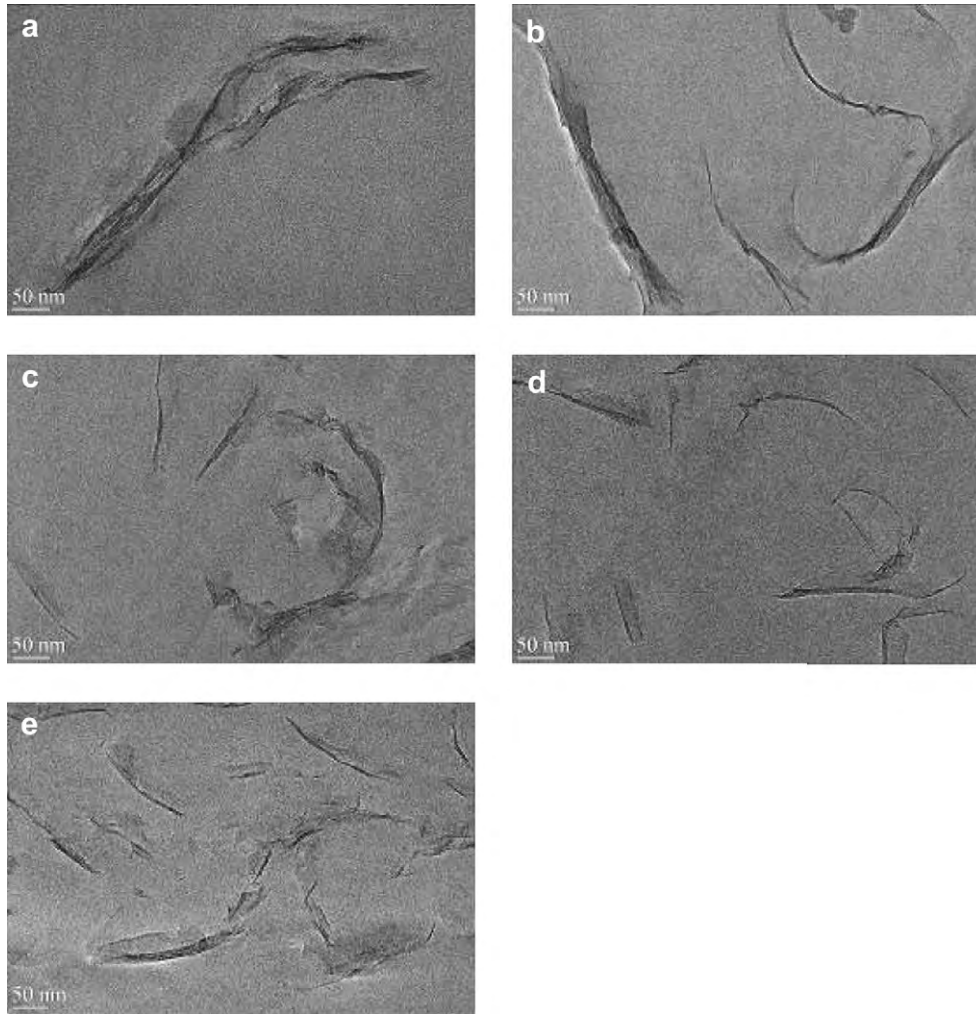


Fig. 2. TEM micrographs of SAN30/20A (95/5) composites prepared from different clay concentrations in THF: (a) 10.0 mg/ml, (b) 7.5 mg/ml, (c) 5.0 mg/ml, (d) 2.0 mg/ml and (e) 1.0 mg/ml at high magnification (40,000).

inferential statistics, the χ^2 test was used in this paper to quantitatively measure the spatial dispersion level of clay in SAN30 using the Matlab code. The standard χ^2 statistic was computed for serial elements (squares in 2D or cuboids in 3D). An element was randomly selected to exclude the effect of a boundary. A threshold was used to determine whether the pixel was SAN30 or clay. $\text{Observed}_{\text{clay_pixels}}$ was the total number of clay pixels in an element. $\text{Uniform}_{\text{clay_pixels}}$ was calculated from the ideal samples, where clay is dispersed in SAN30 uniformly. The χ^2 was calculated by the following equations (1) and (2):

$$\text{Uniform}_{\text{clay_pixels}} = \frac{\text{Number}_{\text{clay_pixels}}}{\text{Number}_{\text{elements}}} \quad (1)$$

$$\chi^2 = \sum_{\text{elements}} \frac{[\text{Observed}_{\text{clay_pixels}} - \text{Uniform}_{\text{clay_pixels}}]^2}{\text{Uniform}_{\text{clay_pixels}}} \quad (2)$$

Another quantitative method for measuring particle dispersion in a polymer, which uses the size of the non-particle-occupied domains rather than the distribution of particles, was developed by Luo et al. [25,26]. A simple MATLAB code was written by Burris et al. to measure the size of non-particle-occupied domains (the free-space length) [27]. In our SAN30/20A nanocomposites, the non-clay-occupied domain size (L_n) is defined as the width of the

largest randomly placed square in 2D images for which the most probable number of clay particles is zero and the details of the calculation are in Ref. [27].

2.3.2. Thermal stability

Thermogravimetric analysis (TGA) was conducted using a TA Instruments TGA Q500 at 5 °C/min from 90 °C to 600 °C in nitrogen (flow rate of 60 cm³/min). Differential scanning calorimetry (DSC) was run in a TA Instruments DSC Q2000 at 10 °C/min from 50 °C to 200 °C in nitrogen (flow rate of 50 cm³/min). The second scan was used for analysis after an initial scan that was followed by cooling. The pans for TGA and DSC were platinum and aluminum, respectively. The samples (≈ 5 mg) for both TGA and DSC were in powder form. The uncertainty of the glass transition temperature was 2.0 °C (2 σ) [28].

Table 1

The density of clay stacks in SAN30/20A (95/5) composites from TEM images.

| Samples | density of clay stacks (μm^2) |
|----------------|--|
| SAN30/20A-10.0 | 16 \pm 8 |
| SAN30/20A-7.5 | 28 \pm 4 |
| SAN30/20A-5.0 | 37 \pm 3 |
| SAN30/20A-2.0 | 50 \pm 5 |
| SAN30/20A-1.0 | 56 \pm 8 |

2.3.3. Flammability-related measurement

A radiant-heating gasification apparatus was designed and constructed at the National Institute of Standards and Technology (NIST) to study the gasification processes of samples by measuring mass loss rates and temperatures of a sample exposed to a fire-like heat flux in a nitrogen atmosphere (no burning) [29]. The apparatus

consists of a stainless steel cylindrical chamber that is 1.70 m tall and 0.61 m in diameter. In order to maintain a negligible background heat flux, the interior walls of the chamber are painted black, and the chamber walls are water-cooled to 25 °C. All experiments were conducted at a radiant heat flux of 50 kW/m². Unlike the cone calorimetry, there is no combustion in the

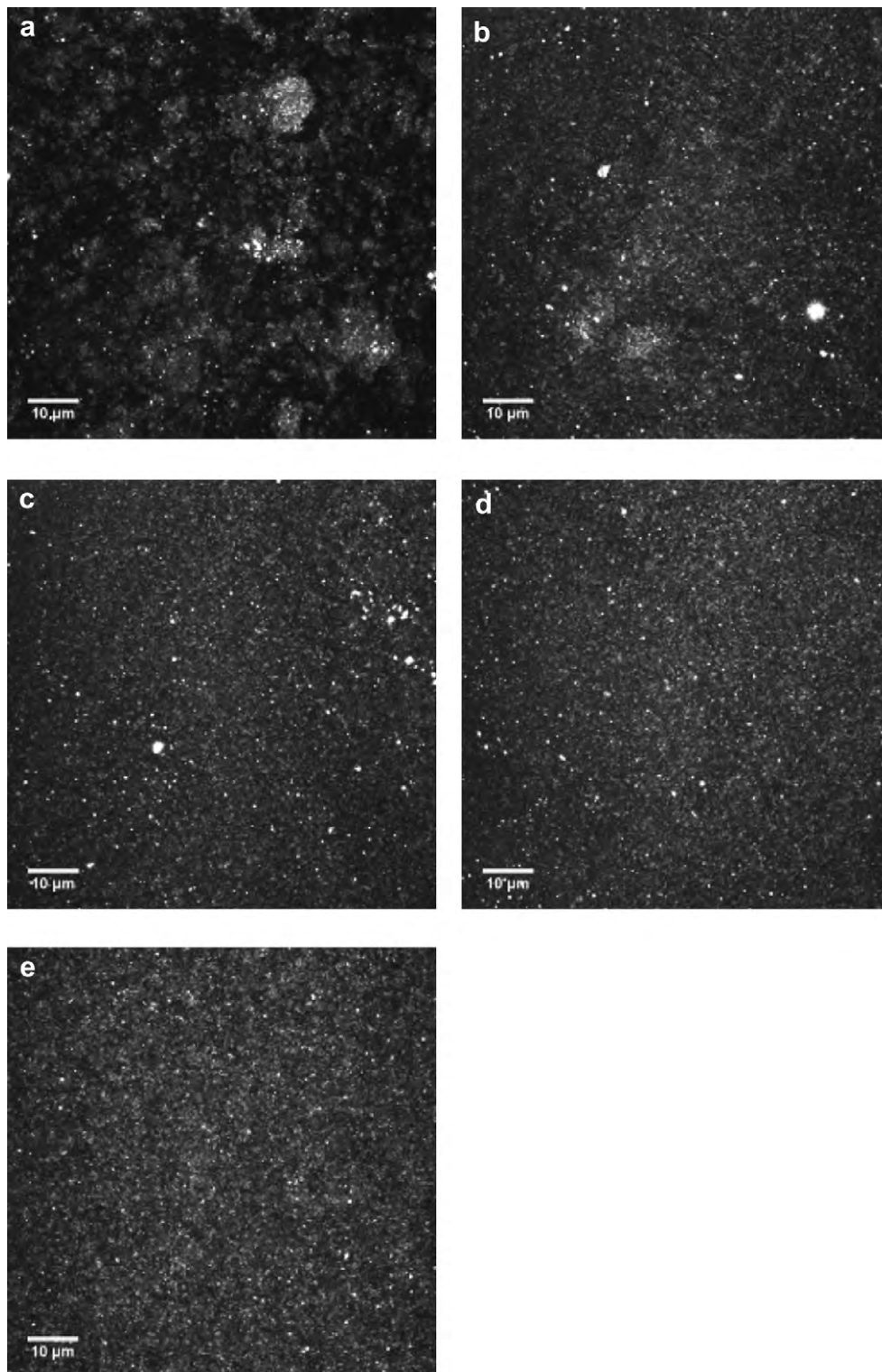


Fig. 3. 2D confocal micrographs of SAN30/20A (95/5) composites prepared from different clay concentrations in THF: (a) 10.0 mg/ml, (b) 7.5 mg/ml, (c) 5.0 mg/ml, (d) 2.0 mg/ml and (e) 1.0 mg/ml.

gasification apparatus. There, observations and results obtained are only based on the condensed phase processes due to the absence of any gas phase oxidation reactions and processes. There is no flame to disturb the view of the condensed phase during the test. The external flux to the sample surface is well-defined, spatially uniform within 3% in the region of 10 cm diameter and nearly constant over the duration of an entire experiment due to the absence of heat feedback from a flame. A more detailed discussion of the apparatus is given in a Ref. [30]. The uncertainties (2σ) of the peak mass loss rate, the total degradation time and the residue yield were $1 \text{ g}/(\text{m}^2\cdot\text{s})$, 6 s and 0.2%, respectively, which were determined by running the pure SAN sample three times.

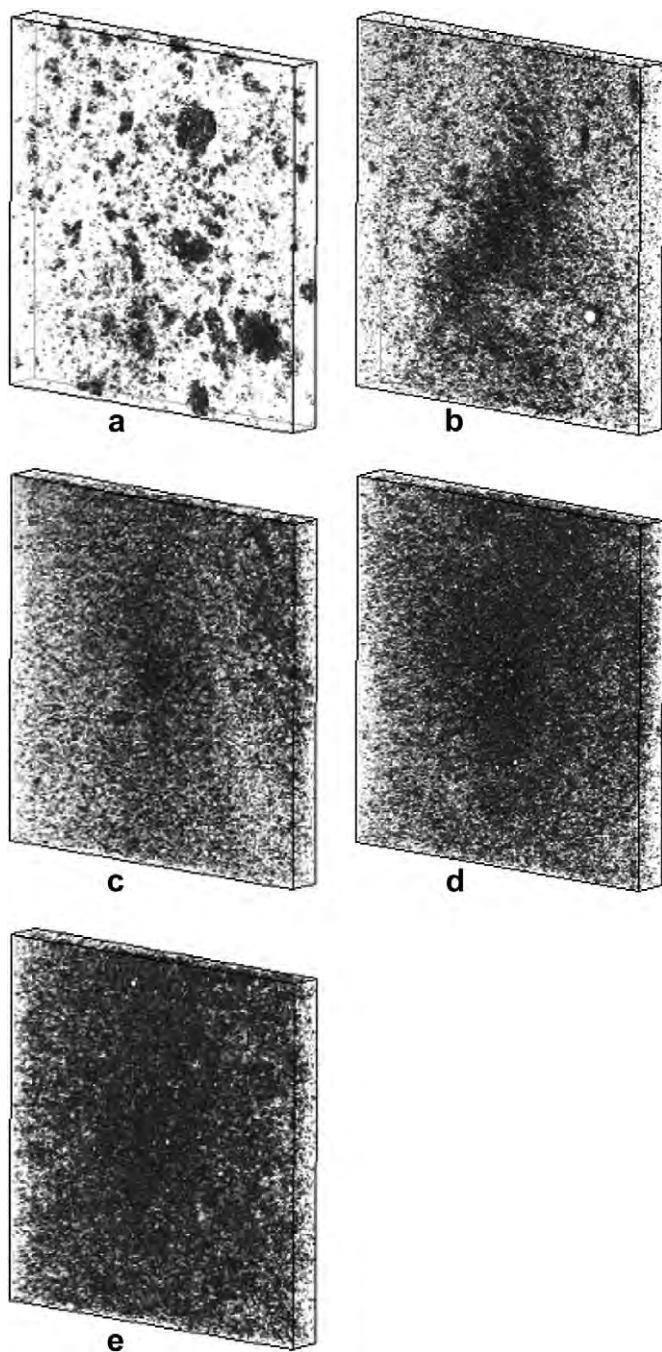


Fig. 4. 3D confocal micrographs of SAN30/20A (95/5) composites prepared from different clay concentrations in THF: (a) 10.0 mg/ml, (b) 7.5 mg/ml, (c) 5.0 mg/ml, (d) 2.0 mg/ml and (e) 1.0 mg/ml.

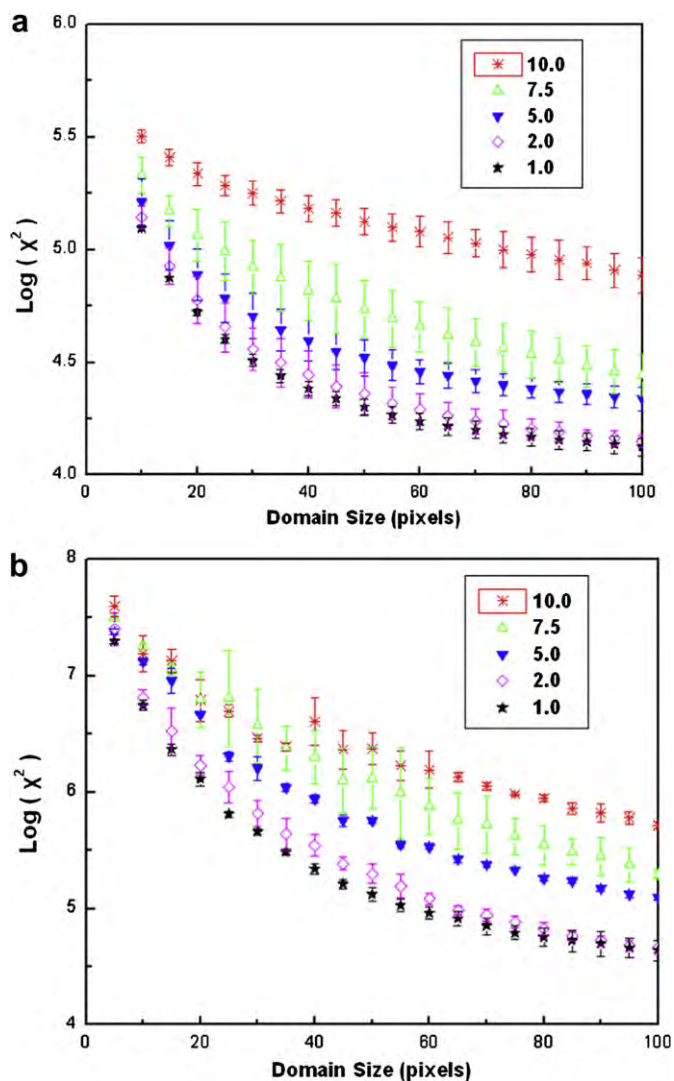


Fig. 5. Standard χ^2 statistic results of SAN30/20A (95/5) composites prepared from different clay concentrations in THF (10.0 mg/ml, 7.5 mg/ml, 5.0 mg/ml, 2.0 mg/ml and 1.0 mg/ml): (a) based on 2D confocal micrographs and (b) based on 3D confocal micrographs.

2.3.4. Characterization of the residues

In order to understand the effect of clay dispersion on the structure of residues from the gasification test, Scanning electron microscopy (SEM) observations of residues were conducted on a Hitachi SU-70 Schottky field emission gun scanning electron microscope working at 5 kV. No coating was applied on the SEM samples to preserve the original morphology of the samples.

2.3.5. Rheology measurement

Rheology measurements were carried out in an AR-G2 AR 2000ex rheometer (TA Instrument) in oscillatory shear with

Table 2

L_n values of SAN30/20As (95/5) composites in 2D confocal micrographs.

| Samples | L_n (μm) |
|----------------|-------------------------|
| SAN30/20A-10.0 | 7.3 ± 0.5 |
| SAN30/20A-7.5 | 4.6 ± 0.6 |
| SAN30/20A-5.0 | 3.3 ± 0.6 |
| SAN30/20A-2.0 | 2.6 ± 0.5 |
| SAN30/20A-1.0 | 1.6 ± 0.4 |

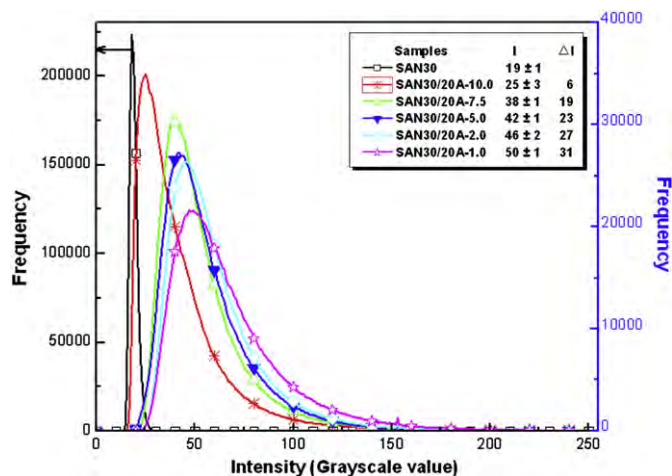


Fig. 6. Relationships between intensity and frequency of SAN30 and SAN30/20A (95/5) composites prepared from different clay concentrations in THF (10.0 mg/ml, 7.5 mg/ml, 5.0 mg/ml, 2.0 mg/ml and 1.0 mg/ml) in 2D projection confocal micrographs.

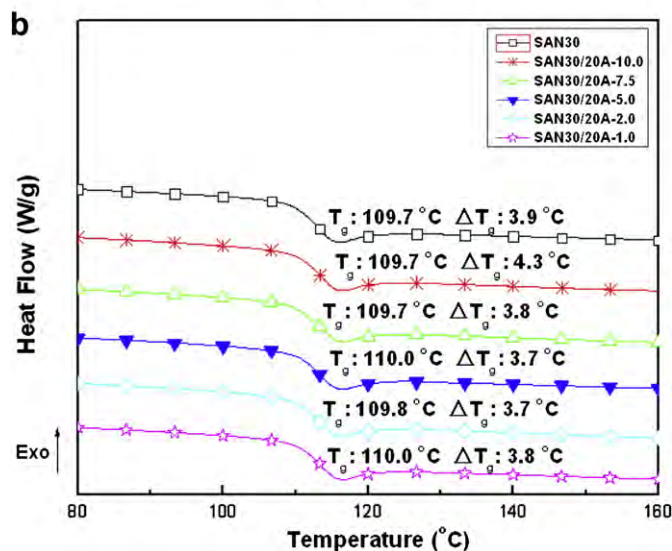
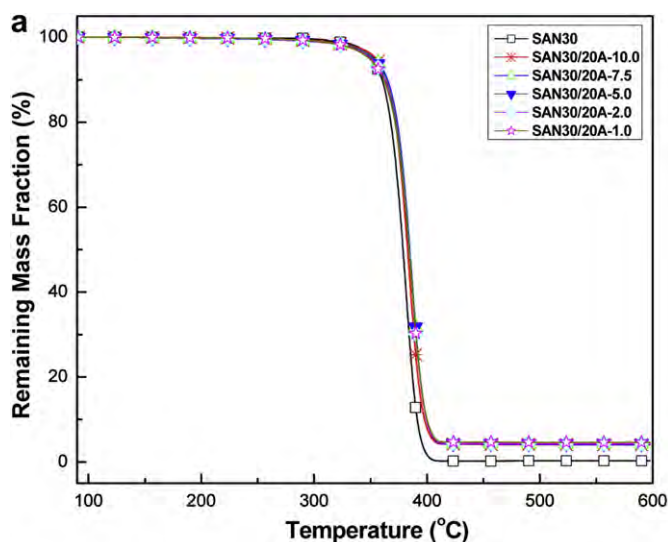


Fig. 7. Thermal properties of SAN30 and SAN30/20A (95/5) composites prepared from different clay concentrations in THF: (a) TGA at 5 °C/min in nitrogen; (b) DSC at 10 °C/min in nitrogen.

a sandwich fixture. A steel plate geometry with a diameter of 25 mm and a gap size of 1.0 mm \pm 0.1 mm were adopted. A temperature sweep was run at an oscillation frequency of 1 rad/s from 180 °C to 260 °C. The constant strain was set at 0.5%, which was verified to be within the linear viscoelastic region (LVR) of the samples by performing stress sweep. All measurements were performed in a nitrogen atmosphere to minimize oxidative degradation of samples at high temperatures. The uncertainty (2σ) of $\log(G')$ was within 6% as determined by running the pure SAN sample three times.

3. Results and discussion

3.1. Structure and morphology

The structure and morphology of SAN30/20A (95/5) composites prepared from variable clay concentrations in THF were investigated by XRD, TEM and LSCM. As shown in Fig.1, two orders of diffraction peaks of Cloisite 20A appear at $2\theta \approx 3.5^\circ$ and $2\theta \approx 7.1^\circ$, corresponding to the d spacing of 25.5 Å. The peaks of SAN30/20A composites shift to lower 2θ values ($2.7^\circ \pm 0.1^\circ$) and the d spacings increase to $33.2 \text{ \AA} \pm 0.6 \text{ \AA}$, indicating that the SAN30 chains have entered the clay galleries, forming an intercalated structure. However, all the d_{001} spacings of the SAN30/20A composites prepared from different clay concentrations in THF are very similar. The clay concentration in THF has little effect on the interlayer distance of the clay platelets.

Fig.2 shows the TEM micrographs of SAN30/20A (95/5) composites at high magnification (40,000). With the clay concentration in THF decreasing, more clay stacks composed of fewer clay platelets can be observed. Single clay platelets can be observed in the 5.0, 2.0 and 1.0 mg/ml samples, indicating that there is some clay exfoliation in these samples. The density of clay stacks, i.e. the number of clay stacks per μm^2 , was computed using at least three TEM micrographs like those in Fig. 2 following the procedure described in the Ref. [31] (any clay stack, including the exfoliated single clay platelets, is also counted as one clay stack.). As shown in Table 1, the density of clay stacks increases with the clay concentration in THF decreasing, which indicates more clay exfoliation and better clay dispersion in the composites.

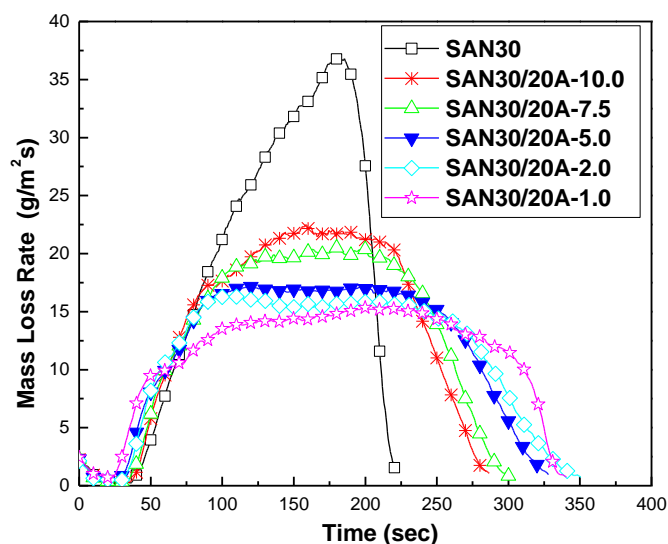


Fig. 8. Mass loss rate of SAN30 and SAN30/20A (95/5) composites prepared from different clay concentrations in THF (10.0 mg/ml, 7.5 mg/ml, 5.0 mg/ml, 2.0 mg/ml and 1.0 mg/ml).

Table 3
Results of the gasification tests.

| Samples | Peak mass loss rate (g/(m ² . s)) | Total time (s) | Residue yield (%) |
|----------------|--|----------------|-------------------|
| Pure SAN30 | 37 | 221 | 0.4 |
| SAN30/20A-10.0 | 22 | 287 | 3.6 |
| SAN30/20A-7.5 | 20 | 300 | 3.7 |
| SAN30/20A-5.0 | 17 | 328 | 3.8 |
| SAN30/20A-2.0 | 16 | 350 | 4.1 |
| SAN30/20A-1.0 | 15 | 340 | 4.3 |

The samples were also characterized by LSCM. Fig. 3 shows the 2D projection micrographs and Fig. 4 shows 3D micrographs constructed with one hundred 2D confocal microscopy images of each sample. White areas represent clay in the 2D projection micrographs while dark areas are clay in 3D micrographs. The images in Figs. 3 and 4 show large clay agglomerations in both 10.0 and 7.5 mg/ml samples, especially in the former while such clay agglomerations are hardly seen in the 2.0 and 1.0 mg/ml samples. The qualitative trend of clay dispersion on a micro-scale from the LSCM micrographs is the same as that from the TEM micrographs on a nano-scale, i.e., the dispersion of Cloisite 20A in SAN30 composites improves with lower Cloisite 20A concentration in THF.

Additional quantitative analyses using the χ^2 test and the measurement of non-clay-occupied domain size (L_n) were conducted in the LSCM micrographs of SAN30/20A composites. The χ^2 values calculated from the five samples are shown in Fig. 5 as a function of the domain size while the L_n values are summarized in Table 2. The χ^2 value reflects the deviation degree of the clay distribution from the ideal one. A lower value of χ^2 indicates the clay distribution is closer to the ideal one. The results from both 2D and 3D images show the same trend. The lower the clay concentration in THF is, the less the χ^2 value, which indicates better clay dispersion in SAN30 composites. On the other hand, L_n represents the characteristic size of the non-clay-occupied domains in SAN30/

20A composites rather than the distribution of clay in SAN30 [27]. A lower L_n value indicates more domains are covered by clay and the extent of clay exfoliation increases. As shown in Table 2, L_n is reduced with the clay concentration in THF decreasing, also indicating a better dispersion level of clay.

The intensity resolution of the 2D projection micrographs is 8 bit, which means the intensity (grayscale value) range is from 0 to 255 (0 represents pure black and 255 means pure white in the grayscale pictures.). In the above two quantitative methods, a threshold (grayscale cutoff point) is defined to determine whether a pixel is SAN30 or clay. Once the threshold is set, pixels with their intensity less than the threshold are considered as pure SAN30 and others are clay. In fact, such a threshold does not exist in the pictures. For the SAN30/20A composites, the XRD shows that the SAN30 chains enter into galleries of clay and the d_{001} spacing of the clay in the composites is about 3 nm. In the 2D pictures, the size of a pixel is about 82 nm \times 82 nm, indicating that the pixels are much larger than the d_{001} spacing. Therefore, every pixel could be shared by both SAN30 and clay, and its intensity is decided by both of them. Thus it is difficult to exactly separate SAN30 from clay by defining a threshold. Strictly speaking, some clay, the intensity of which is less than the threshold, is excluded in both of the above two quantitative methods.

Fig. 6 shows the relationship between the intensity and the frequency of pixels in the 2D projection pictures of pure SAN30 and of the SAN30/20A composites. The curve for SAN30 is mainly in the very low intensity range, and its peak is very high and sharp. The intensity at the maximum pixel frequency for pure SAN30 is only 20 ($I_{peak, SAN30} = 20$). The pixel frequency peaks for the SAN30/20A nanocomposites shift to higher intensity values and the overlap region of their curves with that of pure SAN30 becomes smaller with clay concentration in THF decreasing. When the clay disperses in SAN30, the intensity of a pixel which contains clay will increase since the intensity of reflected light from clay is much stronger than that of pure polymer in the confocal

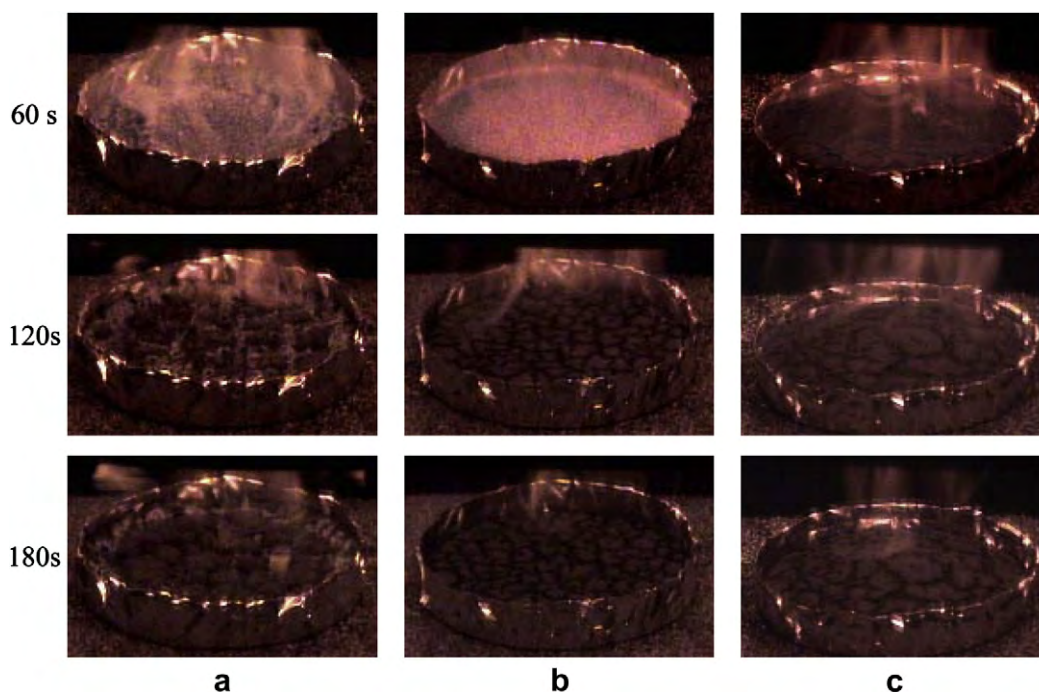


Fig. 9. Gasification behaviors of SAN30/20A (95/5) composites at 60 s, 120 s and 180 s from the start of the test at an external radiant flux of 50 kW/m in nitrogen: (a) SAN30/20A-10.0 mg/ml, (b) SAN30/20A-7.5 mg/ml and (c) SAN30/20A-1.0 mg/ml.

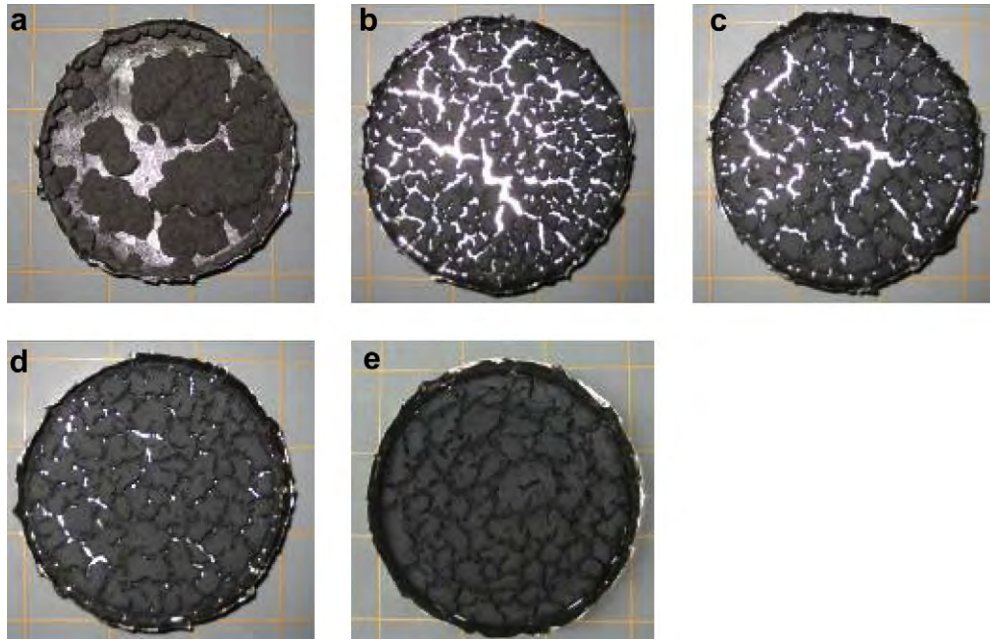


Fig. 10. Residue pictures of SAN30/20A (95/5) composites after the gasification test at an external radiant flux of 50 kW/m^2 in nitrogen: (a) 10.0 mg/ml, (b) 7.5 mg/ml, (c) 5.0 mg/ml, (d) 2.0 mg/ml and (e) 1.0 mg/ml.

microscope. As shown in Table 1 and Table 2, the density of the clay stacks increases with a higher level of clay dispersion and the non-clay-occupied domain is reduced, which makes the intensity of the majority of the pixels increase. Therefore, the shift of the intensity at the maximum frequency (ΔI) compared with pure SAN30, as shown in Fig.6, which represents the change in intensity of the majority of the pixels, can also be used as an additional indication of the level of clay dispersion. ΔI was calculated using the following equation (3):

$$\Delta I = I_{\text{peak_of_SAN30/20A}} - I_{\text{peak_of_SAN30}} \quad (3)$$

From 10.0 mg/ml to 1.0 mg/ml samples, ΔI increases from 6 to 30; again, this indicates the dispersion level of clay in SAN30 composites increases.

From the above qualitative and quantitative results, it is clearly seen that SAN30/20A nanocomposites with different spatial dispersion levels of clay were obtained by controlling the clay concentrations in THF. Compared XRD, TEM with LSCM results, the shift in interlayer distance between clay platelets (Δd_{001}) can be obtained from XRD, which is very useful to measure if the composites is intercalated in most instances. However, it has been reported that the Δd_{001} of polymer nanocomposites with Cloisite

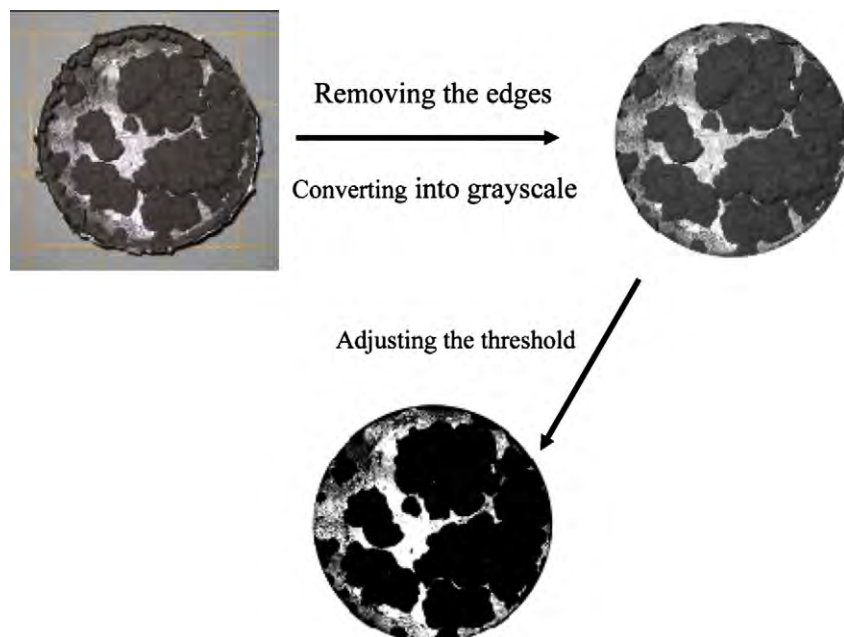


Fig. 11. Process of measuring the area of the cracks by “ImageJ”.

Table 4
Full-depth crack yields calculated using “ImageJ”.

| Samples | $Y_{\text{crack.yield}}$ (%) |
|----------------|------------------------------|
| SAN30/20A-10.0 | 20 |
| SAN30/20A-7.5 | 15 |
| SAN30/20A-5.0 | 8 |
| SAN30/20A-2.0 | 2 |
| SAN30/20A-1.0 | 0 |

15A is almost zero compared with the d_{001} spacing of Cloisite 15A, i.e., 31.5 Å [20,21]. Moreover, the shifts in the d_{001} spacing can not reflect variations in the number of clay platelets in the clay stacks. Therefore, the Δd_{001} does not measure the spatial dispersion of clay. From TEM micrographs at high magnification, one clearly sees the change in the number of clay platelets in clay stacks and in the density of clay stacks at a nano-scale resolution, but the observation area for TEM is extremely small. A much larger sample area can be observed with LSCM at micro-scale resolution, but it is difficult to observe the number of clay platelets in clay stacks. Therefore, XRD and TEM, combined with LSCM can fill up their own deficiencies

and more effectively measure the clay dispersion on both a nano-scale and a micro-scale.

3.2. Thermal stability

The effect of clay dispersion on thermal properties was measured by TGA and DSC. As shown in Fig. 7(a), the TGA curves of SAN30/20A composites are all close to each other, showing little higher stability than pure SAN30 above about 350 °C, probably due to the inorganic components of Cloisite 20A, which do not degrade at higher temperature. DSC results for these samples are shown in Fig. 7(b). The onset of the glass transition (T_o) is taken as T_g of the composites and the temperature change between the onset and the end of the glass transition range ($T_e - T_o$) is denoted as the ΔT_g of the transition. The results show that the clay dispersion does not significantly affect the T_g or ΔT_g , indicating that the motion of the polymer segment is not retarded by the clay. From these TGA and DSC results, the clay dispersion has little effect on the thermal properties of the SAN30/20A composites.

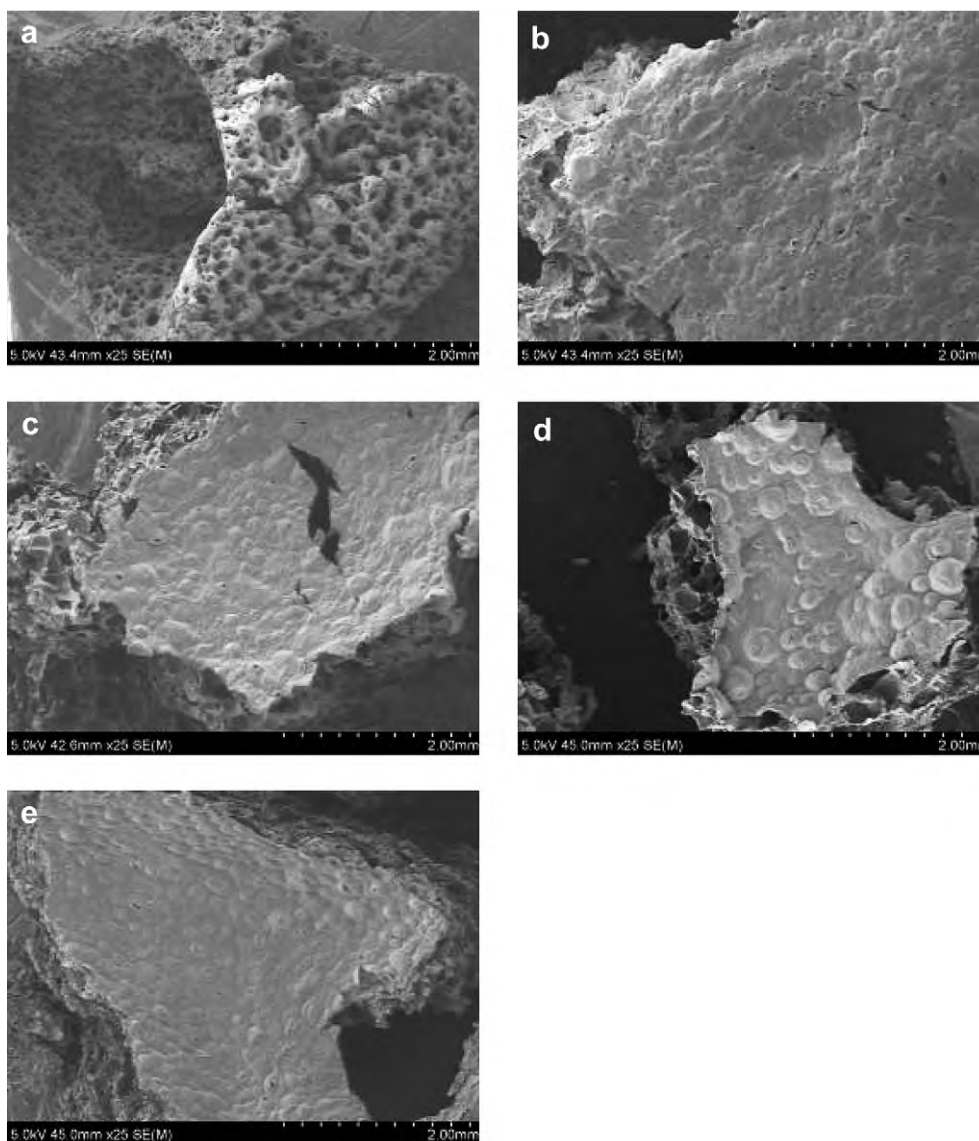


Fig. 12. SEM micrographs of SAN30/20A (95/5) residues after the gasification test at an external radiant flux of 50 kW/m² in nitrogen: (a) 10.0 mg/ml, (b) 7.5 mg/ml, (c) 5.0 mg/ml, (d) 2.0 mg/ml and (e) 1.0 mg/ml.

3.3. Flammability-related properties

The mass loss rate curves of SAN30 and the SAN30/20A nanocomposites at an external radiant flux 50 Kw/m^2 in a nitrogen atmosphere are shown in Fig. 8, and the summary data are listed in Table 3. It is clearly shown that the addition of Cloisite 20A effectively reduces the peak mass loss rate of SAN30. Even for the samples with the high clay concentration in THF (10.0 mg/ml), the peak mass loss rate of SAN30 is reduced by about 40%. Comparing 1.0 mg/ml sample with 10.0 mg/ml sample, one sees that an additional reduction in the peak mass loss rate, approximately 32%, is achieved with the improved clay dispersion. With clay concentration in THF decreasing (improved clay dispersion), the peak mass loss rate decreases monotonically while both the total degradation time and the residue yield increase, which means that the samples prepared from low clay concentration in THF tend to burn slower. The reduction trend of the peak mass loss rate of SAN30 is relatively small when the clay concentration in THF is below 5.0 mg/ml.

3.4. Possible mechanism of the effect of MMT dispersion on flammability properties

For all of the SAN30/20A nanocomposites used in this study, the content of clay in SAN30 is the same (a mass fraction of 5%) and the only difference in these samples is the spatial dispersion level of clay. How the spatial dispersion of clay affects the sample behavior in the simulated fire condition could be observed in the nitrogen gasification process. Selected pictures from the video recordings are shown in Fig. 9. For 10.0 mg/ml samples (the poorest clay dispersion sample in this study), small bubbles, which were formed from thermal degradation products in the molten resin [32], appeared on the surface about 40 s. Large bubbles were formed from the edge of the sample at about 50 s, reaching to the center at about 70 s (Fig. 9(a)) at 60 s). Therefore, the sample behaved like a viscous liquid. At about 90 s, large cracks and solid-like islands were observed on the surface. The solid-like islands, transported by the interstitial bubbles, aggregated with cracks between/among them becoming wider and deeper (Fig. 9(a) at 120 s and 180 s). At the end of the test, the residue consisted of large separate islands in the sample holder as shown in Fig. 10(a). For the 7.5 mg/ml sample (the second poorest clay dispersion), small bubbles appeared at about 50 s and disappeared at about 70 s. As shown in Fig. 9(b), vigorous bubbling was suppressed. Unfortunately, the cracks still became wider and deeper with time increasing. Fig. 10(b) shows that the cracks went through to the bottom of the sample at the end of the test. For 1.0 mg/ml samples (the best clay dispersion sample in this study), shown in Fig. 9(c), small bubbles were completely suppressed before 60 s. Though cracks still appeared, they were limited to the surface and were small compared with other samples (Fig. 10(e)). The behaviors of 5.0 mg/ml and 2.0 mg/ml samples were almost the same as that of 1.0 mg/ml samples except that some cracks went through to the bottom of the samples. These results show that for better dispersion level of clay, there is less bubbling during the gasification test and more uniform residues with less cracking or opening.

The residues collected after the nitrogen gasification test show numerous cracks through the residues. During the gasification test, vigorous bubbling through cracks was observed. Since bubbling is caused by heterogeneous/homogenous nucleation of thermal degradation products of SAN30, the mass loss of the sample is enhanced by the rapid transport of degradation products from the interior of the sample to the surface via the cracks. Therefore, it is important to quantify the crack area and to determine the relationship between the mass loss rate and the total area of the cracks. The crack analysis was carried out on digital photos of each residue

collected after the gasification test. The image analysis software “ImageJ” created by the National Institutes of Health was used to measure the crack area. Each photo was imported into “Image J” and converted into an 8 bit picture. The residue area for analysis was selected by cutting out the edge to exclude the effect of the sample holder. The total area and crack area were calculated by defining a grayscale cutoff point. The process is shown in Fig. 11 and the crack yield was calculated by the following equation (4) and the calculation results are listed in Table 4.

$$Y_{\text{crack_yield}}(\%) = \frac{\text{crack_area}}{\text{total_area}} \times 100\% \quad (4)$$

Here, the cracks which appear on the surface but do not go through the bottom were not calculated in the crack yield. The uncertainty of the method is within 2% (2σ).

Fig. 12 shows SEM micrographs of the top surface of residues from the SAN30/20A composites with different dispersion levels of clay. The structures of all samples residue are similar except for that of the 10.0 mg/ml sample (the poorest clay dispersion sample). There are many small holes in the top surfaces of this residue while the other samples show a more continuous surface. All residues except the poorest clay dispersion sample are foam-like and some bubbles appear on their surface. The foam-like, uniform residues could provide a better physical barrier to act as a heat shield and to reduce the transport of degradation products from the interior of the sample to the surface during the degradation process, thereby reducing the mass loss rate.

Fig. 13 shows the relationships between the normalized peak mass rate loss, the crack yield determined by the equation (4) and the dispersion level of clay quantified by ΔI for five samples. A linear fit was used to correlate the dispersion level of clay with the normalized peak mass rate loss and the crack yield, respectively. The coefficients of determination with the normalized peak mass rate loss and the crack yield are 0.91 and 0.88, respectively, while their P -values are both less than 0.01, which indicates the fits correlate well. The results clearly indicate that a better level of clay dispersion in the polymer composite results in a lesser crack yield and a lower mass loss peak (implying lesser flammability).

The above results demonstrate that the better the dispersion of clay, the fewer cracks there are in sample residues, lowering the mass loss rate. A possible mechanism for the effect of clay dispersion on flammability properties based on these results is then

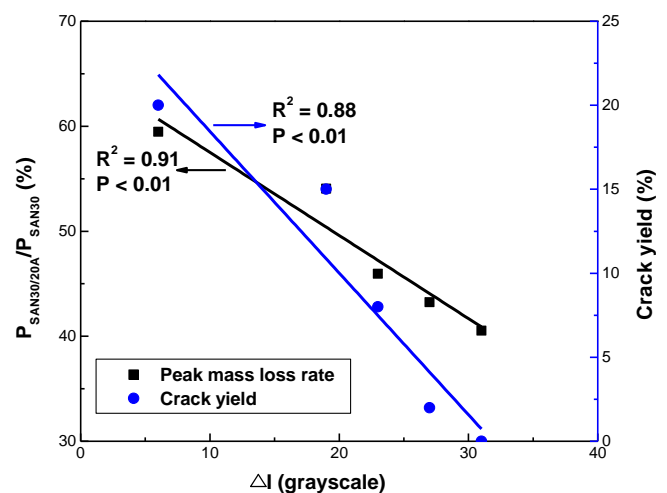


Fig. 13. Relationships between the normalized peak mass loss rate of SAN30/20A (95/5) nanocomposites by the peak mass loss rate of pure SAN30, crack yield and the level of clay dispersion quantified by ΔI .

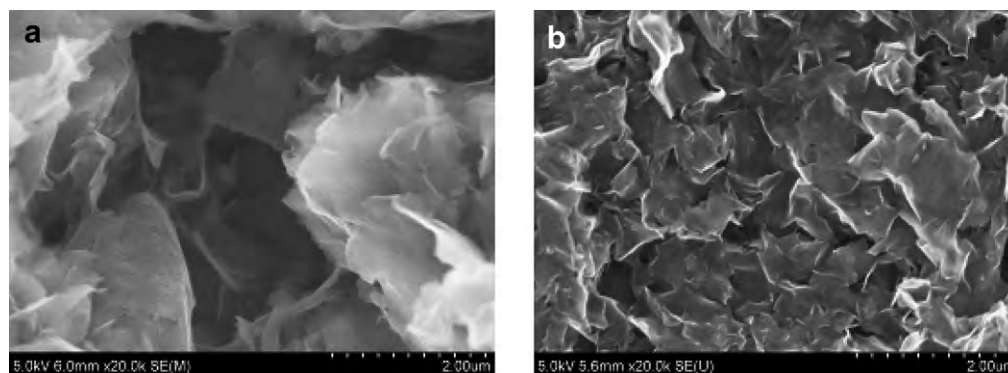


Fig. 14. SEM micrographs of cross section of SAN30/20A (95/5) residues after the gasification test at an external radiant flux of 50 kW/m^2 in nitrogen at high magnification (20,000): (a) SAN30/20A-10.0 mg/ml and (b) SAN30/20A-2.0 mg/ml.

proposed. For the poorer clay dispersion, as shown in Fig. 2(a) and (b), we reasonably hypothesize that there are more domains without clay in the nanocomposites. A significant overlapping of the intensity of 10.0 mg/ml samples and that of pure SAN30 in Fig. 6 also strongly suggests there are some domains with little clay present. When the sample is exposed to heat, the behavior of these domains should be the same as that of pure SAN30, i.e., melting, liquefying and bubbling. Cracks are probably initiated in these domains. On the other hand, Fig. 2 and Table 1 show that the clay stacks are always composed of more clay platelets and the density of clay stacks is lower in the samples with poorer clay dispersion. Therefore, the probability of one clay stack associating with other clay stacks is low, which tends to inhibit the formation of a network structure [33]. Large holes can be seen in the cross sections of 10.0 mg/ml sample residues though there are some clustering of clay stacks at high magnification (Fig. 14 (a)). With a better level of clay dispersion, the non-clay occupied domain is reduced as shown in Table 2. Clay stacks are composed of fewer clay platelets and the density of clay stacks increase shown in Table 1. Smaller non-clay-occupied domains and more clay stacks make it possible for the clay stacks easily associating with each other. In 2.0 mg/ml sample residues (Fig. 14(b)), clay platelets associating with each other and big holes are hardly observed. With more clay particle associations, one expects a stronger network structure to be formed.

Fig. 15 shows results of a temperature sweep in a rheometer of SAN30 and SAN30/20A nanocomposites from $180 \text{ }^\circ\text{C}$ to $260 \text{ }^\circ\text{C}$, which confirm the formation of network in the composites with better clay dispersion. The storage modulus increases with the clay concentration in THF decreasing (better clay dispersion) at a fixed temperature, but the incremental enhancement becomes much less from 5.0 to 1.0 mg/ml samples. Above about $240 \text{ }^\circ\text{C}$, the storage modulus almost becomes independent on the temperature in 2.0 and 1.0 mg/ml SAN30/20A nanocomposites, which indicates a network structure is formed. With more clay stacks associating with each other, the network is physically enough strong that it suppresses bubbling and forms a protective char layer under radiative degradation condition. Therefore, the gaseous degradation products inside probably act as a blowing agent as they do for an intumescent flame retardant (IFR); this makes the samples swell to form foam-like residues, as shown in Fig. 12.

4. Conclusions

In this work, SAN30/20A (95/5) nanocomposites with various spatial dispersion levels of MMT clay were prepared by the coagulation method. The spatial dispersion level of clay in SAN30 is determined using LSCM combined with XRD and TEM. The quantitative results based on TEM and LSCM micrographs show SAN30/20A nanocomposites with different levels of clay dispersion on both a nano-scale and a micro-scale are obtained. However, the Δd_{001} data from XRD does not correctly represent the clay dispersion. A linear fit correlates flammability-related properties and crack yields with the quantified clay dispersion by the shift of the intensity, respectively. In this study, the highest clay dispersion gave a peak mass loss rate (at a 50 kW/m^2 radiant flux) that was 32% lower than the peak for the samples with the lowest clay dispersion. With a better dispersion level of the clay, the density of clay stacks increases and the domains without clay are reduced in size. When the better clay dispersion samples are exposed to heat, the clay stacks easily become entangled with each other and form a network structure. The result is the formation of a uniform residue with fewer cracks or openings, which forms a heat shield and reduces the rate of supply of evolved degradation products to the gas phase, thereby reducing the mass loss rate.

Acknowledgements

M.F.L. acknowledges funding partially from the China State Scholarship and partially from the National Institute of Standards and Technology (NIST). X.Z. acknowledges the support of the Maryland NanoCenter and its NispLab. The NispLab is supported in

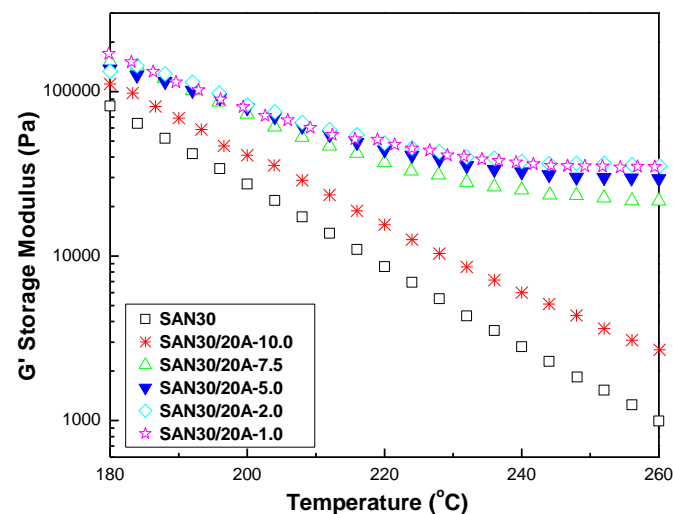
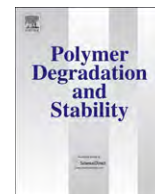


Fig. 15. Temperature sweep of SAN30 and SAN30/20A (95/5) composites prepared from different clay concentrations in THF (10.0 mg/ml, 7.5 mg/ml, 5.0 mg/ml, 2.0 mg/ml and 1.0 mg/ml).

part by the NSF as an MRSEC Shared Experimental Facility. T. K. acknowledges funding from the NIST under Grant 9H9184. We gratefully acknowledge Dr. Zhouhui Lian and Dr. Songfeng Wu, Dr. Li-Piin Sung and Dr. Tom Ohlemiller and at the NIST for helping with discussing the calculation of clay dispersion and writing the Matlab code, the confocal microscopy test and grammatical corrections, respectively.

References

- [1] Usuki A, Kojima Y, Kawasumi M, Okada A, Kurauchi T, Kamigaito O. Abstracts of Papers of the American Chemical Society 1990;200:218.
- [2] Ray SS, Okamoto M. Progress in Polymer Science 2003;28:1539.
- [3] Morgan AB. Polymers for Advanced Technologies 2006;17:206.
- [4] Wilkie CA, Zheng XX, Chigwada G, Costache M, Jang BN, Zhang JG. In: CANGI Wilkie, editor. Amer Chemical Soc; 2006. p. 8.
- [5] Gilman JW, Jackson CL, Morgan AB, Harris R, Manias E, Giannelis EP, et al. Chemistry of Materials 2000;12:1866.
- [6] Zhu J, Uhl FM, Morgan AB, Wilkie CA. Chemistry of Materials 2001;13:4649.
- [7] Stretz HA, Wootan MW, Cassidy PE, Ko JH. Polymers for Advanced Technologies 2005;16:239.
- [8] Samyn F, Bourbigot S, Jama C, Bellayer S, Nazare S, Hull R, et al. European Polymer Journal 2008;44:1631.
- [9] Samyn F, Bourbigot S, Jama C, Bellayer S. Polymer Degradation and Stability 2008;93:2019.
- [10] Yoo Y, Paul DR. Polymer 2008;49:3795.
- [11] Wu YP, Huang HH, Zhao W, Zhiang HF, Wang YQ, Zhang LQ. Journal of Applied Polymer Science 2008;107:3318.
- [12] Berta M, Saiani A, Lindsay C, Gunaratne R. Journal of Applied Polymer Science 2009;112:2847.
- [13] Miltner HE, Watzzeels N, Block C, Gotzen NA, Van Assche G, Borghs K, et al. European Polymer Journal 2010;46:984.
- [14] Morgan AB, Harris JD. Polymer 2003;44:2313.
- [15] Fornes TD, Yoon PJ, Hunter DL, Keskkula H, Paul DR. Polymer 2002;43:5915.
- [16] Xidas PI, Triantafyllidis KS. European Polymer Journal 2009;46:404.
- [17] Do XH, Yu HO, Wang Z, Tang T. Polymer Degradation and Stability 2009;95:587.
- [18] Wang Z, Du XH, Yu HO, Jiang ZW, Liu J, Tang T. Polymer 2009;50:5794.
- [19] Morgan AB, Gilman JW. Journal of Applied Polymer Science 2003;87:1329.
- [20] Dennis HR, Hunter DL, Chang D, Kim S, White JL, Cho JW, Paul DR. Polymer 2001;42:9513.
- [21] Lee MH, Dan CH, Kim JH, Cha J, Kim S, Hwang Y, Lee CH. Polymer 2006;47:4359.
- [22] Du FM, Fischer JE, Winey KI. Journal of Polymer Science Part B-Polymer Physics 2003;41:3333.
- [23] Bellayer S, Gilman JW, Eidelman N, Bourbigot S, Flambard X, Fox DM, et al. Advanced Functional Materials 2005;15:910.
- [24] Kashiwagi T, Fagan J, Douglas JF, Yamamoto K, Heckert AN, Leigh SD, et al. Polymer 2007;48:4855.
- [25] Luo ZP, Koo JH. Journal of Microscopy 2007;225:118.
- [26] Luo ZP, Koo JH. Polymer 2008;49:1841.
- [27] Khare HS, Burris DL. Polymer 2010;51:719.
- [28] Zammarrano M, Franceschi M, Bellayer S, Gilman JW, Meriani S. Polymer 2005;46:9314.
- [29] Austin PJ, Buch RR, Kashiwagi T. Fire and Materials 1998;22:221.
- [30] Ilhan S, Kahruman C, Yusufoglu I. Journal of Analytical and Applied Pyrolysis 2007;78:363.
- [31] Chavarria F, Paul DR. Polymer 2004;45:8501.
- [32] Kashiwagi T. Symposium (International) on Combustion 1994;25:1423.
- [33] Kashiwagi T, Mu MF, Winey K, Cipriano B, Raghavan SR, Pack S, et al. Polymer 2008;49:4358.



Flame retardancy of poly(styrene-co-acrylonitrile) by the synergistic interaction between clay and phosphomolybdate hydrates[☆]

Meifang Liu^{a,b,*}, Xin Zhang^c, Mauro Zammarano^a, Jeffrey W. Gilman^a, Takashi Kashiwagi^{a,*}

^a Fire Research Division, National Institute of Standards and Technology, Gaithersburg, MD 20899, United States

^b The State Key Laboratory of Polymer Materials Engineering, Polymer Research Institute of Sichuan University, Chengdu 610065, China

^c Department of Materials Science and Engineering, University of Maryland, College Park, MD 20742, United States

ARTICLE INFO

Article history:

Received 30 July 2010

Received in revised form

9 December 2010

Accepted 16 January 2011

Available online 3 February 2011

Keywords:

Clay

Flame retardant

Phosphomolybdate

Poly(styrene-co-acrylonitrile)

ABSTRACT

A combination of montmorillonite (MT) clay and catalysts was used to explore possible synergistic effects in reducing the flammability of poly(styrene-co-acrylonitrile) (SAN). Several catalysts, including ammonium phosphomolybdate hydrate (NHPMo), melamine phosphomolybdate hydrate (MEPMo), zinc phosphomolybdate hydrate (ZnPMo) and sodium phosphomolybdate hydrate (NaPMo), were used. The combination of MT (Cloisite 20A) with NHPMo showed synergistic enhancement in improving the char formation and reducing the peak mass loss rate of SAN40 as compared with SAN40 composites containing MT or NHPMo alone, while similar synergistic performance was not obtained between MT and NaPMo or ZnPMo or MEPMo. The better flame retardancy with this combination is probably due to the two primary aspects. One is the increased catalytic activity of the combination of Cloisite 20A and NHPMo probably due to the overlapping degradation temperature range of the combination of 20A/NHPMo and SAN40, which probably results in more char formation; the other is more NHPMo being around or on the clay stacks while less is in the galleries of the clay; this probably bridges the clay stacks and strengthens the clay network with char formed during the degradation process. High temperature rheological data confirmed the formation of a stronger network structure in SAN40/20/NHPMo; this benefits flame retardancy by allowing fewer cracks to form in the outer char layer on the polymer mass. The more continuous char layer suppresses bubbles transport of fuel vapors and heat transfer through the char layer, thereby reducing the mass loss rate.

© 2011 Elsevier Ltd. All rights reserved.

1. Introduction

Montmorillonite (MT) clay has been extensively studied as a flame retardant in polymer resins because of its ability to reduce polymer flammability at relatively low add-on levels [1–6]. The MT particles appear to retard heat transfer in the condensed phase and reduce the supply of evolved degradation products to the gas phase, thereby significantly reducing the peak release heat rate of the burning polymer. However, the total heat release is not significantly reduced. It has been reported that the flame retardancy of polymer nanocomposites with clay alone is not sufficient to achieve the requirements of industry, such as meeting requisite performance

levels in the UL-94 standard [7,8]. Further reduction in flammability of polymer/clay nanocomposites is needed for potential industrial applications [9,10].

In general, the formation of char, which remains in the condensed phase during burning, reduces the supply of carbon to the flame and hence reduces heat release rate and total heat release. However, the addition of MT clay particles does not always enhance the formation of char [11]. The polymer/clay nanocomposites do burn more slowly, but most of the polymer is eventually consumed. It has been reported that some catalysts, such as Lewis acids, Friedel-Crafts alkylation reagents, etc., can improve the char yield of a polymer [12–19]. So catalysts of this nature, used in polymer/clay nanocomposites, might be expected to improve the flame retardancy. Our previous research has indicated that a significant amount of char was obtained using zinc chloride in poly(acrylonitrile-co-styrene) (SAN). However, there was no desired synergism with MT clay on flame retardancy, presumably because the char was formed in the later stages of the pyrolysis [19].

[☆] This study was carried out by the National Institute of Standards and Technology (NIST), an agency of the US Government which, by statute, is not subject to copyright in the US.

* Corresponding authors.

E-mail addresses: meifang.liu@nist.gov (M. Liu), takashi.kashiwagi@nist.gov (T. Kashiwagi).

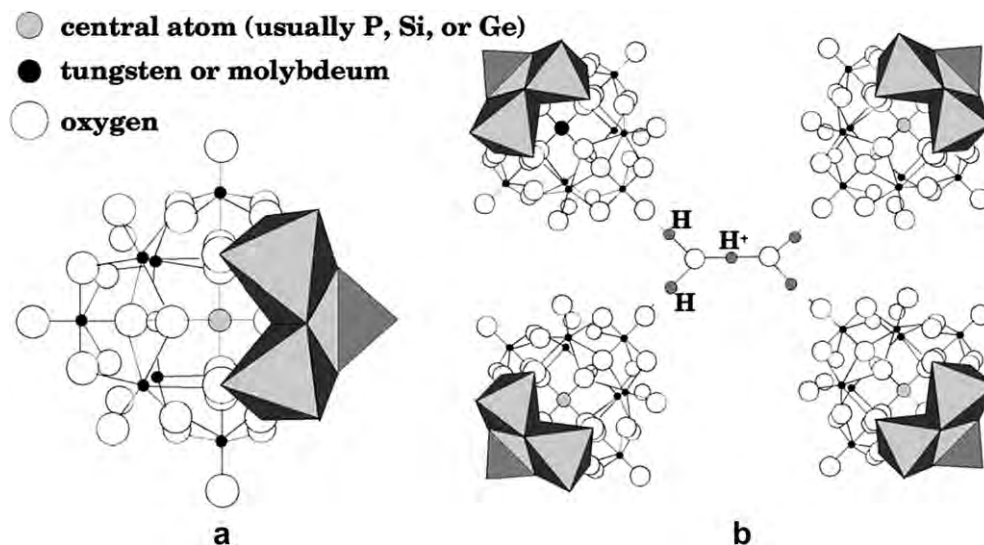


Fig. 1. Structure of HPA: (a) primary structure; (b) secondary structure [The figure is from reference [22]].

Heteropoly acids (HPA) and their salts, polyoxometalates (POM), are an extensive class of polyoxoanions formed by group V and VII metals [20,21]. The primary structure of HPA is the Keggin structure shown in Fig. 1 (a) [22]. Taking the $[\text{PMo}_{12}\text{O}_{40}]^{3-}$ anion for example, P is located in the center of a tetrahedral arrangement of oxygen atoms; the atoms of the transition metal Mo are bound to oxygen atoms, O; twelve oxygen–molybdenum octahedra, form a cage that surrounds the central atom, P. In HPA hydrates, hydronium ions such as H_3O^+ bridge these anions (Fig. 1 (b)). POMs are formed by partial or complete substitution of hydronium ions. Both HPA and POMs are used widely as homogeneous and heterogeneous catalysts in organic synthesis due to their acid–base, multielectron redox properties and their ability to stabilize organic intermediates [23–25], but the use of HPA and POM in the flame retardant field was initiated in Ref. [26].

In this paper, phosphomolybdates (PMo) with different cations, including ammonium phosphomolybdate hydrate (NHPMo), melamine phosphomolybdate hydrate (MEPMo), zinc phosphomolybdate hydrate (ZnPMo) and sodium phosphomolybdate hydrate (NaPMo), were used as catalysts, combined with MT clay, to flame retard SAN. Some protons still remain in the PMo salts even if they are prepared stoichiometrically; these are responsible for its catalytic activity [21]. Moreover, both NHPMo and MEPMo could release (locally) non-reactive gases during their degradation in the condensed phase, which may make the char layer intumesce, thereby helping retard the transfer of heat. ZnPMo, combining both Lewis and Bronsted acids, was expected to produce more char. NaPMo was used as a reference. With this in mind, we examine whether there is a synergistic effect between the clay and each catalyst in improving the flame retardancy of SAN40, and we compare their relative effectiveness.

2. Experimental section

2.1. Materials

SAN40 (styrene-60: acrylonitrile-40) was provided from Asahi Kasei, Japan; Organoclay (Cloisite 20A)¹ treated with dimethyl, dehydrogenated tallow, quaternary ammonium chloride surfactant,

was provided by Southern Clay Products, Inc.; Tetrahydrofuran (THF) was purchased from Fisher Scientific; Phosphomolybdic Acid (HPMo) and NHPMo were purchased from Sigma–Aldrich, Inc.; NaPMo, zinc acetate dihydrate (ZnC) and melamine (ME) were purchased from Fluka, Alfa Aesar and DSM Melamine Americas Inc., respectively; MEPMo and ZnPMo were synthesized according to the literature [27,28].

2.2. Preparation of MEPMo and ZnPMo

ME was dissolved in boiling distilled water to form a clear solution. Then, a solution containing a stoichiometric amount of the parent acid HPMo was added dropwise to a ME solution with stirring. The mixture was continuously stirred for about 30 min. After it cooled, the precipitate was filtered and dried in a vacuum oven at 100 °C. ZnPMo was prepared by a similar procedure without the filtration due to its solubility in water.

2.3. Preparation of samples

The SAN40 composites were prepared by a solvent casting method. SAN40 was dissolved in THF (250 ml). Appropriate amounts of clay and catalysts were added to the SAN40-THF solution while continually stirring. This mixture was sonicated for 1 h and then stirred for 24 h. Then, the mixture was cast into an aluminum foil pan and the THF evaporated overnight in a chemical hood. The mixture was further dried in a vacuum oven at 80 °C for 24 h. The dried sample was ground using a portable coffee grinder. The powder was dried in a vacuum oven at 80 °C overnight. The sample was annealed in a vacuum oven at 160 °C for 1 h as a final drying procedure. The content of Cloisite 20A and PMo in SAN30 composites were kept at 5 mass% and 3 mass%, respectively. The 20A/PMo (5/3) mixture for XRD was prepared by a similar procedure.

All samples for TEM and rheology (discs of 25 mm diameter × 1 mm thickness) and for measuring flammability properties (discs of 75 mm diameter × 4 mm thickness) were compression molded using a Carver press in the range of 170 °C–180 °C under a pressure of about 1.4 MPa for a duration of 15 min.

2.4. Characterization

The X-ray diffraction data (XRD) were collected on a Bruker D8 Advance with a Cu K α tube and 12 mm variable slit at a step size of

¹ Certain commercial equipments, instruments, materials, services or companies are identified in this paper in order to specify adequately the experimental procedure. This in no way implies endorsement or recommendation by NIST.

0.01665° and time step of 0.75 s. The samples of the composites for XRD were the same as the samples for rheology while the samples of clay and 20A/PMo mixtures were powder ground in a mortar.

Transmission electron microscopy (TEM) was conducted with a JEOL JEM 2100F TEM working at 200 kV with a Gatan CCD camera. The TEM sample was prepared with a Leica UC-6 ultramicrotome with a Diatome diamond knife at room temperature. NaPMo and ZnPMo samples were microtomed by dry cutting to prevent the catalysts from dissolving into water. NHPMo and MEPMo samples were microtomed by a water method. The thickness of sections was thinner than 100 nm.

Thermogravimetric analysis (TGA) was conducted using a TA Instruments TGA Q500 at 5 °C/min from 90 °C to 600 °C in nitrogen (flow rate of 60 cm³/min) for the original samples (about 5 mg) in a platinum pan. The samples of the 20A/PMo mixture for TGA were prepared by mixing them in a mortar.

Rheology measurements were carried out on an AR-G2 AR 2000ex rheometer (TA Instruments) in oscillatory shear with a sandwich fixture. In the rheological test, a steel plate geometry with a diameter of 25 mm and a gap size of about 1.0 mm were adopted. For a temperature range between 160 °C and 360 °C, temperature ramp tests at 1 °C/min were conducted at a shear oscillation frequency of 1 rad/s and a constant strain of 0.5%, which was verified to be in the linear viscoelastic region (LVR) of the samples by performing stress sweeps. All measurements were performed in a nitrogen atmosphere to minimize oxidative degradation of samples at high temperatures.

2.5. Flammability property measurements

A radiant-heating gasification apparatus, somewhat similar to a cone calorimeter, was designed and constructed at NIST to study the gasification processes of samples by measuring mass loss rate and temperatures of a sample exposed to a fire-like heat flux in a nitrogen atmosphere (no burning) [29]. The apparatus consists of a stainless-steel cylindrical chamber that is 1.70 m tall and 0.61 m in diameter. In order to maintain a negligible background heat flux, the interior walls of the chamber are painted black and the chamber walls are water-cooled to 25 °C. All experiments were conducted at a radiant heat flux of 50 kW/m². The unique features of the apparatus are: (1) observation and results obtained from it are only based on the condensed phase processes due to the absence of any gas phase oxidation reactions and processes; (2) it enables visual observations of gasification behavior of a sample, using a video camera, under a radiant flux similar to that of a fire without any optical interference from a flame; (3) the external flux to the sample surface is well-defined, spatially uniform within 3% in a region 10 cm in diameter and nearly constant over the duration of an entire experiment due to the absence of heat feedback from a flame. A more detailed discussion of the apparatus is given in a reference [30]; the standard relative uncertainty of the measured mass loss rate is ±10%.

3. Results

3.1. Sample morphology

Fig. 2 provides the XRD patterns of the Cloisite 20A, 20A/PMo mixtures and SAN40 composites. For the Cloisite 20A, two strong characteristic diffraction peaks appear at $2\theta = 3.5^\circ$ and $2\theta = 7.1^\circ$, corresponding to the d spacing of 25.5 Å and 12.4 Å, respectively. For the 20A/PMo mixtures, all the peaks shift slightly to lower 2θ values compared to that of 20A. The d_{001} spacings of 20A/NHPMo, 20A/MEPMo, 20A/ZnPMo and 20A/NaPMo are 28.8 Å, 28.3 Å, 29.2 Å and 29.0 Å, respectively, which are larger than that of 20A. It is due

to probably PMo salts intercalating into the clay, strongly associating with the clay. For SAN40 composites, the d_{001} spacings of SAN40/20A/NHPMo, SAN40/20A/MEPMo, SAN40/20A/ZnPMo and SAN40/20A/NaPMo composites are 30.0 Å, 28.4 Å, 28.7 Å and 29.3 Å, respectively, which are close to those of the 20A/PMo mixtures but less than that of the SAN40/20A composites. The likelihood of SAN40 intercalation is reduced probably due to the strong interaction between clay and PMo. However, the TEM images of SAN40/20A/PMo (92/5/3) and SAN40/20A (95/5) composites at high magnification are similar. As shown in Fig. 3, single clay layer and multi-layer clay stacks are observed, so the SAN40/20A/PMo samples are still considered to be nanocomposites.

3.2. Thermal stability

The TGA curves of the additives by themselves and of the SAN40 and SAN40 composites are shown in Figs. 4 and 5, respectively. The residue of the SAN40 composites not only includes carbonaceous char, but also contains the residue from the additives. In order to evaluate any catalytic char formation enhancement by each additive to SAN40, the residue produced by the additives themselves is first calculated. The calculated residue amount of SAN40 composites is the sum of each component residue amount in the sample without considering the catalytic role of the additives. So the char yield is calculated by the following equations:

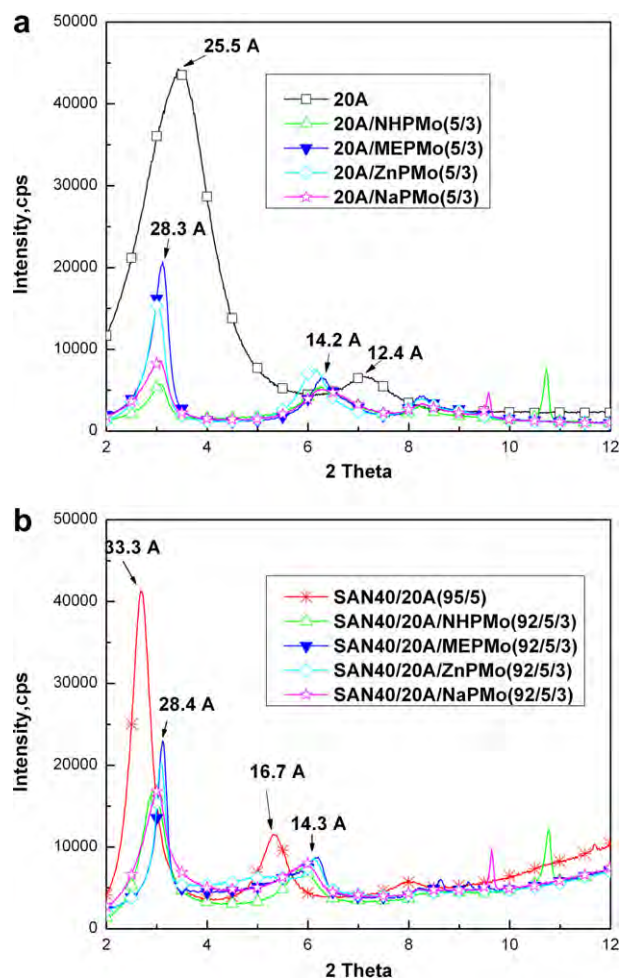


Fig. 2. XRD curves: (a) additives and (b) SAN40 composites.

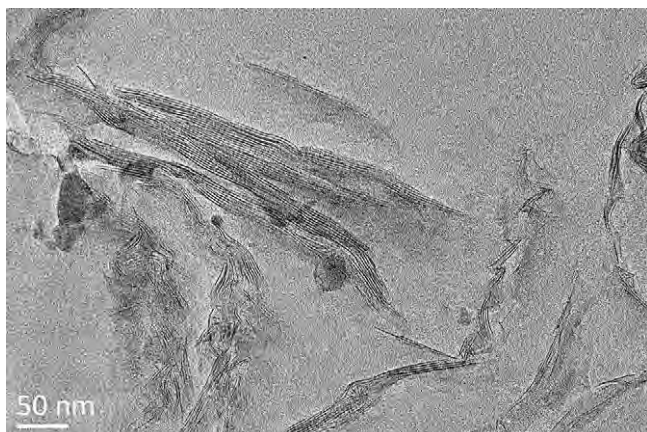


Fig. 3. TEM images of SAN40/20A/NHPMo (92/5/3) composites at high magnification (40,000).

$$Y_{\text{residue_cal}}(\%) = (R_{\text{SAN40}} \times 0.5\% + \sum R_{\text{additive}} \times Y_{\text{additive}}) \times 100 \quad (1)$$

$$Y_{\text{char}} = Y_{\text{residue_ex}} - Y_{\text{residue_cal}} \quad (2)$$

$$Y_{\text{char}}^{\text{combination_inc}} = Y_{\text{char}}^{\text{SAN40/20A/PMo}} - Y_{\text{char}}^{\text{SAN40/PMo}} - Y_{\text{char}}^{\text{SAN40/20A}} \quad (3)$$

Where R is the mass weight percent in the composites and 0.5% is the char yield of SAN40. The third equation above calculates the actual increment of carbonaceous char seen with a given additive combination due to any synergism among the ingredients. The residue yields of additives (Y_{additive}) including Cloisite 20A, NHPMo, NaPMo, ZnPMo and MEPMo are 62.0%, 93.7%, 97.9%, 94.6% and 73.2%, respectively (Fig. 4). The calculation results are presented in Table 1 and plotted in Fig. 6.

As shown in Fig. 5, the degradation of pure SAN40 occurs in a single step (300–400 °C); it is known to proceed via local chain scission followed by propagating β -scission with evolved volatiles including acrylonitrile, styrene, benzene and toluene, leaving little carbonaceous char (0.5%) [31]. With 5% clay, the residue increases but most of it is the inorganic components of Cloisite 20A. The char yield is only 1.2%, signifying that the catalytic effect of clay on the char formation of SAN40 is not significant. The thermal stability of

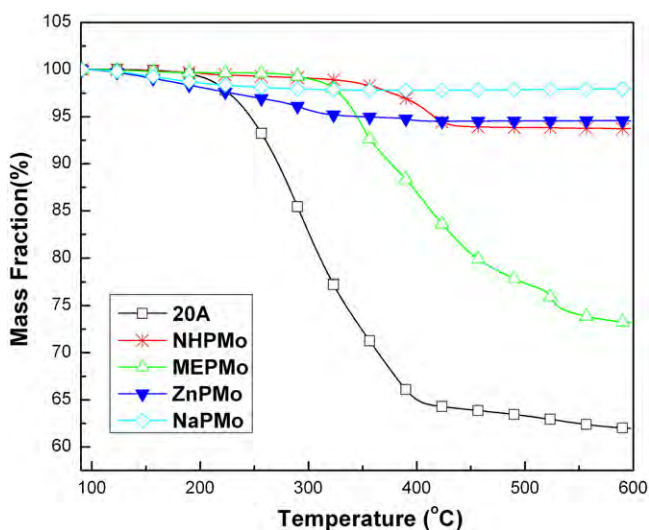


Fig. 4. TGA curves of Cloisite 20A and PMo salts in nitrogen at 5 °C/min heating rate.

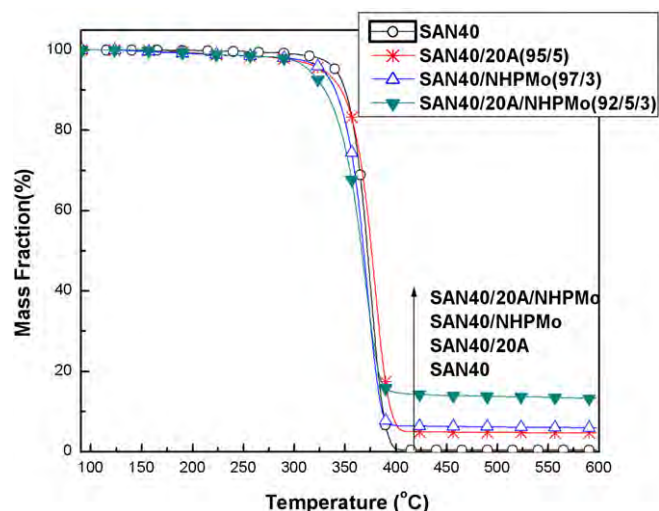


Fig. 5. TGA curves of SAN40 and SAN40 composites in nitrogen at 5 °C/min heating rate.

SAN40/NHPMo (97/3) is similar to, though slightly less than, that of SAN40, and yields a little more char (2.6%). The combination of Cloisite 20A and NHPMo further reduces the thermal stability of SAN40 below 400 °C but produces about 6.8% char, which is more than the 1.2% char yield of SAN40/20A (95/5) and the 2.6% char yield of SAN40/NHPMo (97/3). These results indicate that there is a synergism between 20A and NHPMo that enhances the char produced from SAN40. The effects of the other catalysts on the TGA curves of SAN40 and SAN40/20A composites are almost the same as that of NHPMo except for different residue yields. From the calculation results shown in Table 1 and Fig. 6, the char yield produced by the other catalysts is more than that of SAN40/NHPMo but the increase in the char yield due to the combination of 20A and MEPMo or ZnPMo or NaPMo is almost zero, which indicates no synergism was shown between 20A and MEPMo or ZnPMo or NaPMo.

3.3. Flammability properties

The effects of the additives on the mass loss rate of SAN40 in the gasification apparatus are shown in Fig. 7. The mass loss starts earlier and ends earlier with the addition of the PMo salts,

Table 1
TGA and calculation data of SAN40 composites at 600 °C.

| Sample | $Y_{\text{residue_ex}}^a$ (%) | $Y_{\text{residue_cal}}^b$ (%) | Y_{char}^c (%) | $Y_{\text{char}}^{\text{combination_inc}d}$ (%) |
|-----------------------------|-----------------------------------|------------------------------------|----------------------------|---|
| SAN40/20A(95/5) | 4.8 | 3.6 | 1.2 | / |
| SAN40/NHPMo(97/3) | 5.9 | 3.3 | 2.6 | 3.0 |
| SAN40/20A/ NHPMo(92/5/3) | 13.2 | 6.4 | 6.8 | |
| SAN40/MEPMo(97/3) | 9.7 | 2.7 | 7.0 | −0.6 |
| SAN40/20A/ MEPMo(92/5/3) | 13.4 | 5.8 | 7.6 | |
| SAN40/ZnPMo(97/3) | 8.0 | 3.3 | 4.7 | 0.6 |
| SAN40/20A/ ZnPMo(92/5/3) | 12.9 | 6.4 | 6.5 | |
| SAN40/NaPMo(97/3) | 8.5 | 3.4 | 5.1 | −0.7 |
| SAN40/20A/ NaPMo(92/5/3) | 12.1 | 6.5 | 5.6 | |

^a Experimental residue yield.

^b Calculated residue yield.

^c Char yield produced by the additives.

^d Char yield increased by the combination.

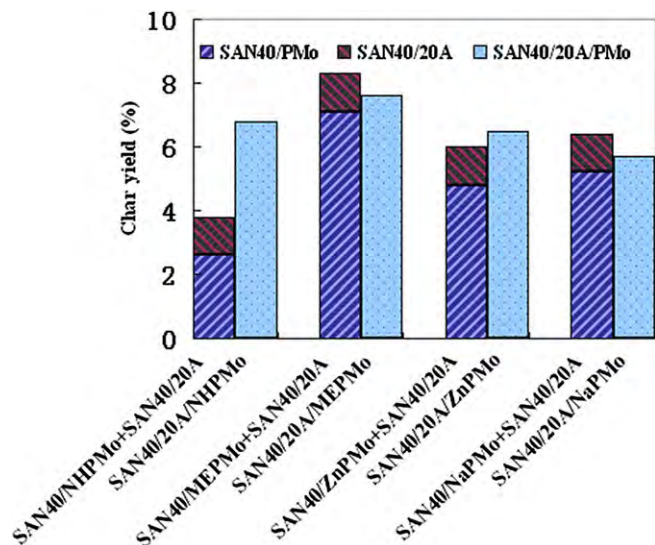


Fig. 6. Char yields of SAN40/20A (95/5), SAN40/PMo (97/3) and SAN40/20A/PMo (92/5/3) composites.

indicating that PMo salts make SAN40 degrade earlier; this agrees with the TGA results shown in Fig. 5. However, the PMo salts, except MEPMo, have no significant effect on reducing the peak mass loss rate of SAN40. As shown in Fig. 4, MEPMo starts to decompose at about 300 °C in the TGA and could release a lot of gases potentially acting as blowing agents in the char; this would increase the porosity of the char layer, tending to reduce heat transferred through the char [32]. Moreover, the TGA results also show that more char is obtained by the catalytic performance of MEPMo. Therefore, MEPMo reduces the peak mass loss rate of SAN40 from 37 g/(m² s) to 30 g/(m² s), implying better flame retardancy. Although NHPMo also can release gases during its degradation, the peak mass loss rate is not reduced probably due to less gas and less char.

Cloisite 20A by itself effectively retards the mass loss of SAN40 as indicated in Fig. 7 (b), and the observed behavior is further affected by the addition of some of the PMo salts. The peak mass loss rate of SAN40 is reduced about 30% with the addition of Cloisite 20A. However, there is no further significant reduction of the peak mass loss rate in the SAN40 with Cloisite 20A when NaPMo or ZnPMo are added. The peak mass loss rate of SAN40/20A/MEPMo composites is slightly less than that of SAN40/20A composites. However, for the SAN40/20A/NHPMo composites, the peak mass loss rate is about 15 g/(m² s), which is much less than that of SAN40/NHPMo (34 g/(m² s)) and SAN40/20A (25 g/(m² s)), again, indicating that NHPMo has a synergistic effect with 20A.

4. Discussion

The above results show that the combination of Cloisite 20A and NHPMo not only enhances the char yield of SAN40, but also reduces the peak mass loss rate. It is of interest to determine why only the combination of 20A and NHPMo shows this synergism effect among the combinations used in the study.

The TGA and DTG curves of Cloisite 20A, 20A/PMo mixtures are shown in Fig. 8. The maximum degradation rate of Cloisite 20A is delayed by the addition of PMo salts. This is probably due to the stabilizing effect of heteropolyanions on the quaternary ammonium chloride surfactant in Cloisite 20A. As shown in Table 2, the residue yields of 20A/NHPMo and 20A/MEPMo are higher than the calculated residue yields, indicating that NHPMo and MEPMo can

make the organic modifier in clay form char. Compared to that of the combination of Cloisite 20A and other PMo salts, the thermal stability of 20A/MEPMo is still lower over the whole test temperature range probably due to the much lesser thermal stability of MEPMo itself. It is clearly seen in the DTG curves that the degradation processes of 20A/NaPMo, 20A/ZnPMo and 20A/MEPMo occur over a wide temperature range with the maximum degradation peak at about 300 °C while the degradation of 20A/NHPMo is mainly from 300 °C to 400 °C with the maximum degradation peak at about 344 °C, which is close to the degradation peak of pure SAN40 (The pure SAN40 mainly degrades in 300 °C–400 °C with the maximum degradation peak at about 375 °C shown in Fig. 5). There are thus probably more reactions among 20A/NHPMo, SAN40 and their degradation products due to this overlap in degradation temperature range, leading to more char. However, the details of the reaction mechanism are not clear and further study is needed.

With the combination of 20A and the catalysts, the dispersion of additives in SAN40 composites is also probably changed. There are some agglomerations of clay stacks as shown in Fig. 9, especially in SAN40/20A/MEPMo and SAN40/20A/NaPMo samples. This poorer dispersion of clay stacks brings negative effects on flammability. For the catalysts, there are three possible locations of for the PMo catalysts in SAN40/20A/PMo composites: (1) away from the clay stacks; (2) around or on the clay stacks and (3) in the galleries of clay. As shown in Fig. 9 (b), many NHPMo particles around or on clay

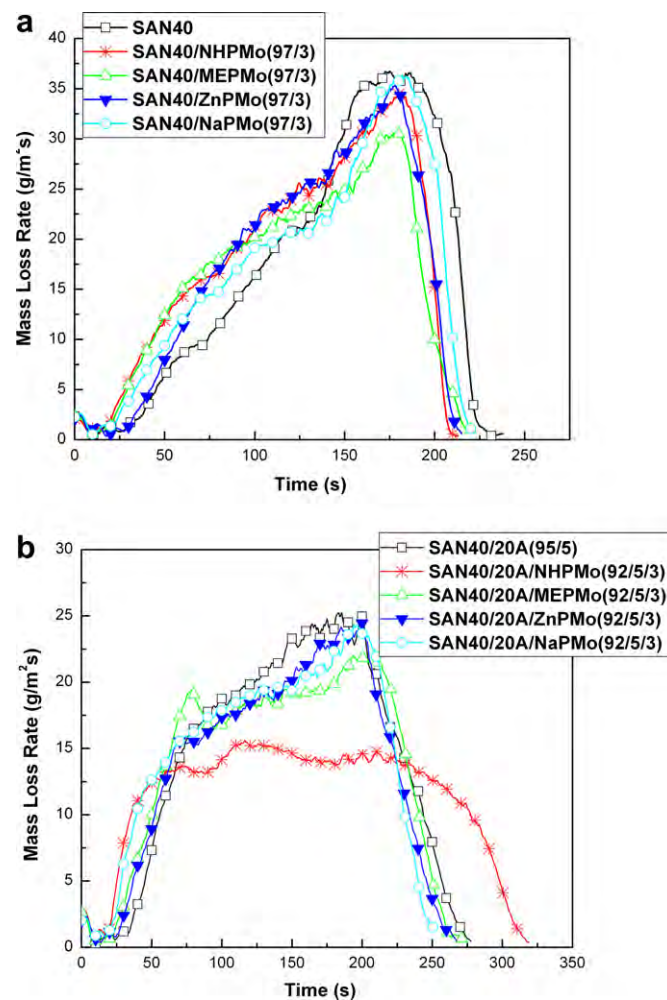


Fig. 7. Mass loss rate curves from the gasification test: (a) SAN40 and SAN40/PMo (97/3) composites; and (b) SAN40/20A (95/5) and SAN40/20A/PMo (92/5/3) composites.

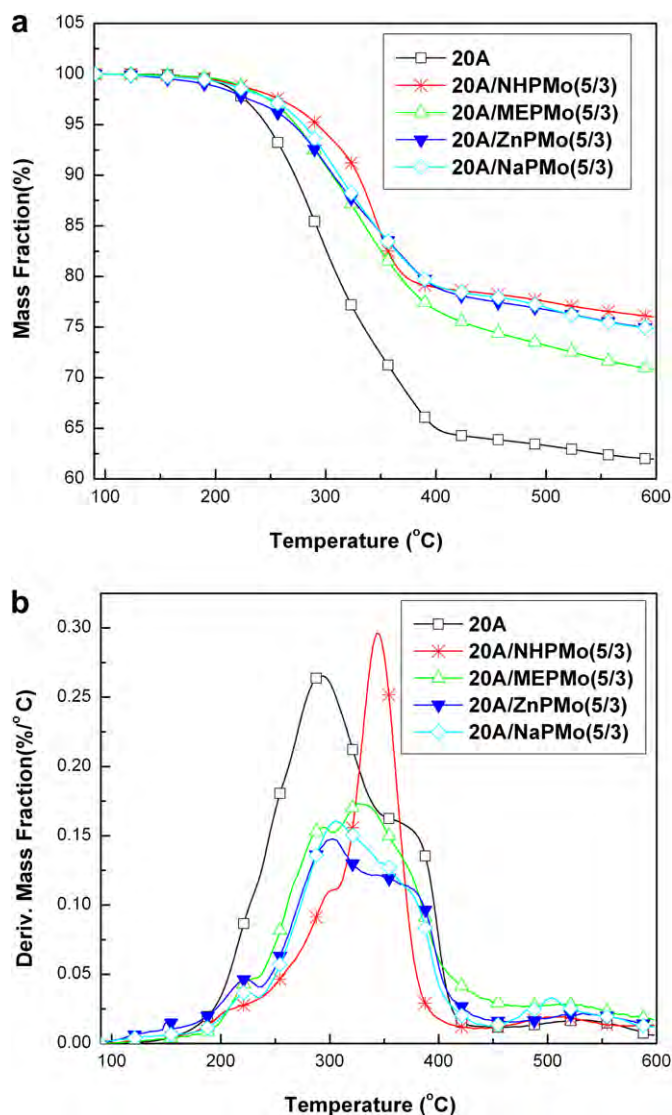


Fig. 8. TGA results of 20A, 20A/PMo mixtures in nitrogen at 5 °C/min heating rate: (a) TGA curves and (b) DTG curves.

stacks are observed in SAN40/20A/NHPMo composites but similar associations are not observed in other samples. The char will be formed around clay stacks when catalysts are around them; this probably bridges the space between clay stacks and strengthens the clay network. Moreover, the catalytic role of the portion of the catalyst adsorbed on the clay surface may be improved due to its increased surface area. However, if the catalysts are in the galleries of the clay, they cannot play any role in char formation of SAN40 since the polymer chains have difficulty entering into in these galleries in SAN40/20A/PMo samples. The solubility of NHPMo in THF is much less than that of other catalysts, so the amount of

Table 2
TGA data of 20A/PMo (5/3) mixtures at 600 °C.

| Samples | Experimental residue yield (%) | Calculated residue yield (%) | Residue yield increased by the combination (%) |
|-----------|--------------------------------|------------------------------|--|
| 20A/NHPMo | 76.0 | 73.9 | 2.1 |
| 20A/MEPMo | 70.8 | 66.2 | 4.6 |
| 20A/ZnPMo | 74.9 | 74.2 | 0.7 |
| 20A/NaPMo | 74.8 | 75.5 | −0.7 |

NHPMo in the galleries is less. Therefore, one expects less NHPMo in the galleries of clay and more around or on the clay stacks; again, this probably bridges the clay stacks and strengthens clay network with char formed during the gasification test.

From the TGA results, the main degradation process of SAN40 composites occurs in the temperature range of 300 °C–400 °C. Temperature-ramp rheology tests were carried out over a wide temperature range, 160 °C–360 °C, which is close to the degradation temperature of the composites, to see if there is a network structure formed in this range. The results are shown in Fig. 10. With increasing temperature, the storage modulus of pure SAN40 decreases essentially monotonically. The storage modulus is close to zero when the temperature is about 350 °C. When the 20A clay is added, the storage modulus becomes higher compared to that of pure SAN40 at any fixed temperature, indicating an increase in “rigidity”. For the SAN40/20A/PMo composites, the temperature-dependent behavior of the storage modulus is different from that of both SAN40 and SAN40/20A composites. A peak appears in the high temperature range of about 260 °C–360 °C, which indicates some crosslinking reactions occur and network structures are formed in this temperature range.

The beginning temperature of the peak (T_b), the peak temperature (T_p) and the peak storage modulus (G_p) are used here to describe this peak. These data are listed in Table 3. The SAN40/20A/NHPMo composites not only show higher T_b and T_p , but also have the largest G_p . Moreover, the rate of decrease in the storage modulus after the peak for this composite is slower than that for the others, indicating a slower breakdown of the network. Even at 360 °C, the storage modulus of SAN40/20A/NHPMo composite is about two orders of magnitude higher than that of the others. The stronger network structure is thus probably preserved at higher temperatures and for a longer time, which confirms that the NHPMo provides a beneficial strengthening of the clay network. For the SAN40/20A/NaPMo, SAN40/20A/ZnPMo and SAN40/20A/MEPMo composites, network structures are mainly formed in the range from 260 °C to 300 °C, lower than that of the SAN40/20A/NHPMo composites. Although the peak storage modulus values of SAN40/20A/ZnPMo and SAN40/20A/MEPMo are higher than that of SAN40/20A/NaPMo, the rates of decrease of the modulus after the peak of the former are faster than that of the latter. At 360 °C, all their storage modulus values are close to that of the SAN40/20A nanocomposites, indicating a breakdown of the network structure. The destruction of the network structure at higher temperature probably has a negative effect on the formation of continuous protective layer, without cracks, on the heated exterior of a polymer mass [33].

Fig. 11 shows how the residue of SAN40 composites is formed during a gasification test. For the SAN40/20A (95/5) composites (Fig. 11 (a)), bubbles which are formed from thermal degradation products in the molten resin [34] appear on the top of the entire sample from 30 s to 50 s and then become less extensive as solid-like clumps appear. Many cracks appear in the clumps at around 60 s which then get deeper and deeper. The whitish plumes in these pictures are not flames, but aerosols from evolved gaseous degradation products. Some solid-like clumps, transported by the interstitial bubbling process, aggregate, yielding some carbonaceous islands as shown in the pictures of the final residues (Fig. 12 (b)). Compared with SAN40 samples, the addition of Cloisite 20A reduces the bubbling but does not suppress it completely.

With 20A and NHPMo both present, the color darkens a little earlier than it does in the case of the SAN40/20A composites. Some big bubbles appear at around 15 s but break slower, indicating that the degradation to the gas phase becomes slower. Some solid-like clumps appear and bubbling is still observed at round 30 s. From

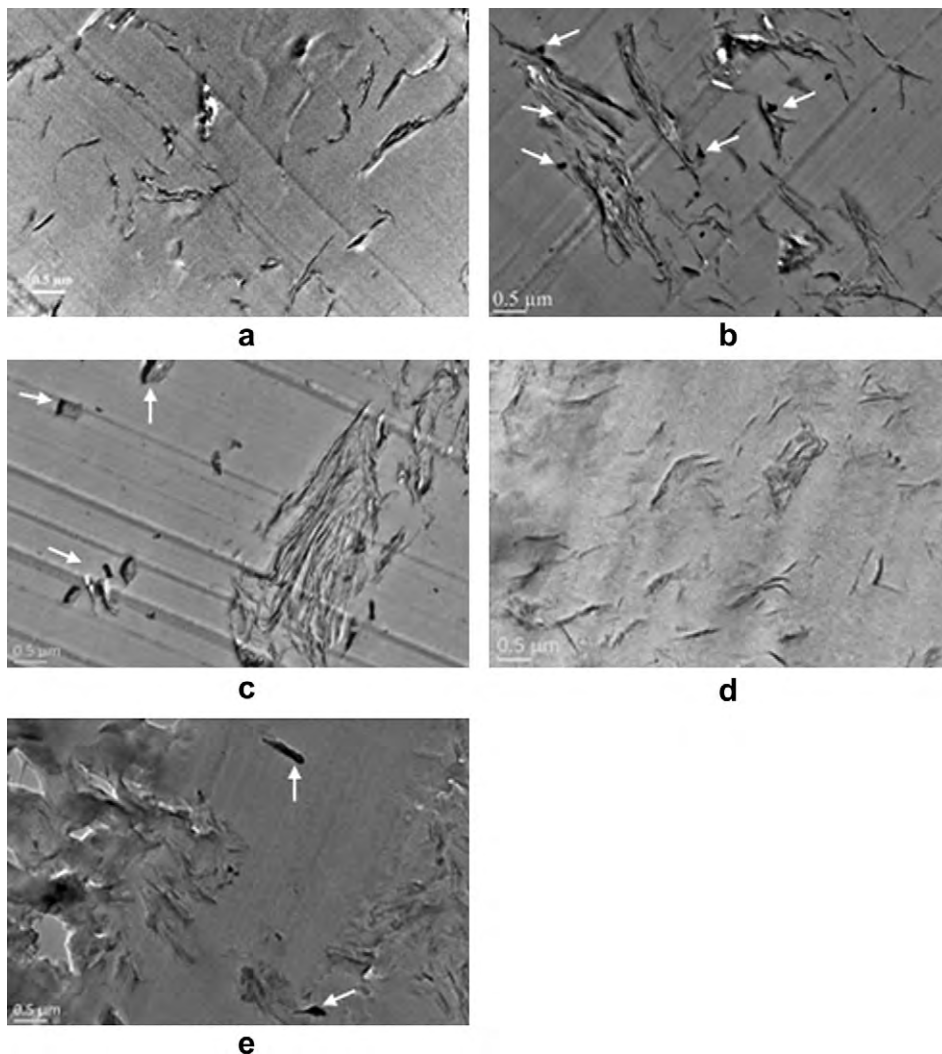


Fig. 9. TEM images of SAN40 composites at low magnification (4000): (a) SAN40/20A (95/5); (b) SAN40/20A/NHPMo (92/5/3); (c) SAN40/20A/MEPMo (92/5/3); (d) SAN40/20A/ZnPMo (92/5/3); and (e) SAN40/20A/NaPMo (92/5/3).

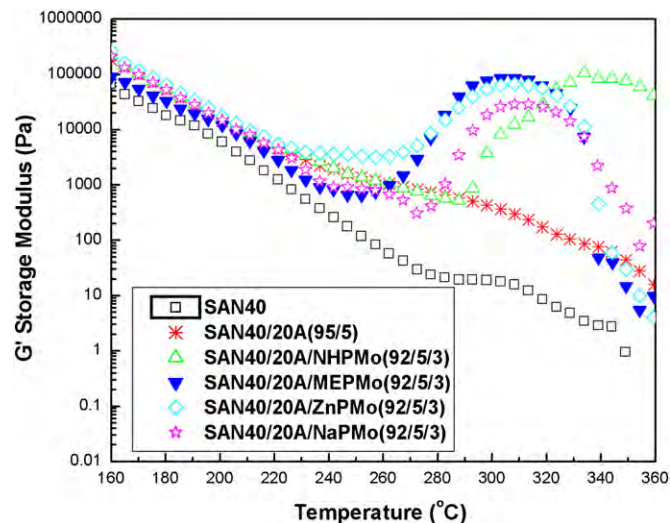


Fig. 10. Temperature ramps of SAN40 and SAN40 composites in nitrogen.

60 s to 120 s (Fig. 11 (b)), the solid-like residue increases, covering the whole sample; this could suppress vigorous bubbling and prevent degradation products from escaping from the sample to the gas phase [35]. Moreover, the whitish plumes become less, indicating degradation products are released slower. Therefore, the degradation products may have more time to make contact with the NHPMo catalyst, which also could increase the residue yield (Table 4). After about 180 s, there are no bubbles and no cracks on the surface. The residue shown in Fig. 12 (c) indicates that the coherent carbonaceous protective layer does not breakdown even at the end of the test, probably due to its stronger network structure, which is more effective to suppress the bubbling.

For the SAN40/20A/NaPMo, SAN40/20A/ZnPMo and SAN40/20A/MEPMo composites, the gasification behavior of each is almost the same. Taking SAN40/20A/ZnPMo for example (Fig. 11 (c)), some

Table 3
Peak data of the temperature ramp test in nitrogen.

| Samples | T_b (°C) | T_p (°C) | G_p (10^4 Pa) |
|-------------------------|------------|------------|--------------------|
| SAN40/20A/NHPMo(92/5/3) | 287.8 | 333.9 | 10.1 |
| SAN40/20A/MEPMo(92/5/3) | 250.0 | 303.2 | 8.8 |
| SAN40/20A/ZnPMo(92/5/3) | 231.1 | 308.2 | 6.7 |
| SAN40/20A/NaPMo(92/5/3) | 272.6 | 308.2 | 2.8 |

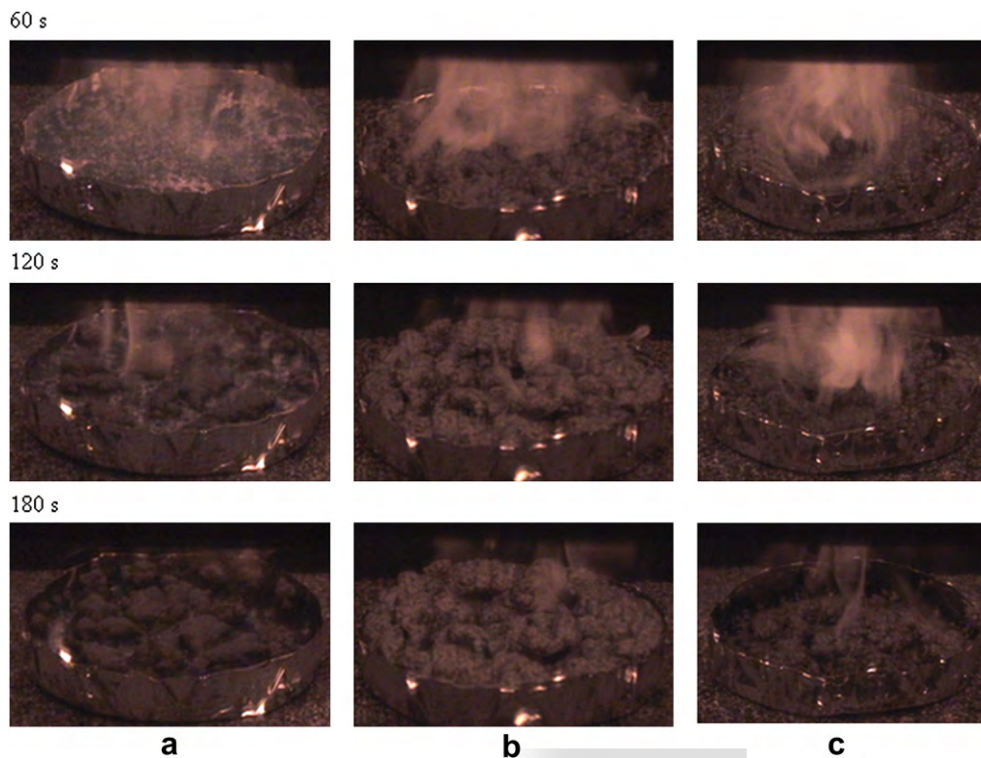


Fig. 11. Gasification behavior of at 60 s, 120 s and 180 s from the start of the test at an external radiant flux of 50 kW/m in nitrogen: (a) SAN40/20A (95/5), (b) SAN40/20A/NHPMo (92/5/3) and (c) SAN40/20A/ZnPMo (92/5/3).

solid-like clumps appear first during the gasification process and then cracks appear, probably due to destruction of network structures at higher temperatures. Evidently, the solid-like clumps aggregate. Vigorous bubbling from the thermal degradation is

observed emerging through the cracks during the gasification process. Some cracks still appear in the residue (Fig. 12 (e)). Therefore, the mass loss rate shows no significant reduction compared with SAN40/20A composites.

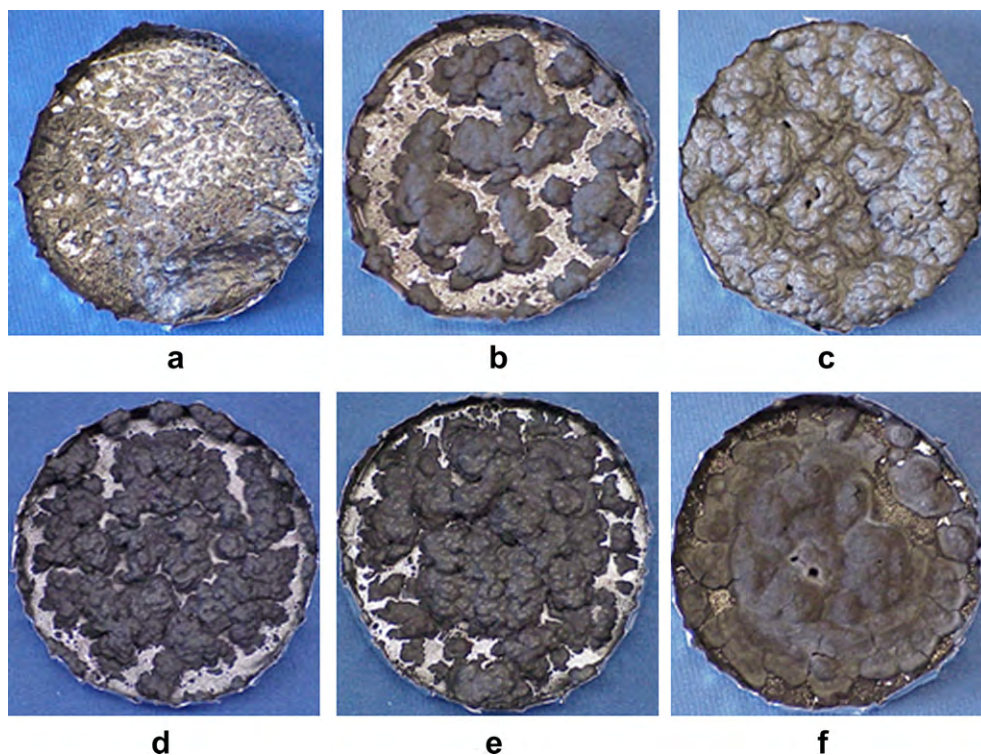


Fig. 12. Pictures of the residues collected after the gasification test at an external radiant flux of 50 kW/m² in nitrogen: (a) SAN40; (b) SAN40/20A (95/5); (c) SAN40/20A/NHPMo (92/5/3); (d) SAN40/20A/MEPMo (92/5/3); (e) SAN40/20A/ZnPMo (92/5/3) and (f) SAN40/20A/NaPMo (92/5/3).

Table 4

Gasification residue yields of SAN40 composites.

| Sample | Residue yield (%) |
|-------------------------|-------------------|
| SAN40/NHPMo(97/3) | 5.8 |
| SAN40/20A/NHPMo(92/5/3) | 12.4 |
| SAN40/MEPMo(97/3) | 7.6 |
| SAN40/20A/MEPMo(92/5/3) | 11.3 |
| SAN40/ZnPMo(97/3) | 8.6 |
| SAN40/20A/ZnPMo(92/5/3) | 12.3 |
| SAN40/NaPMo(97/3) | 6.1 |
| SAN40/20A/NaPMo(92/5/3) | 10.4 |

5. Conclusions

A synergistic enhancement between MMT clay and NHPMo in improving the flame retardancy of SAN40 is obtained. The combination of Cloisite 20A with NHPMo not only enhances the char yield of SAN40, but also reduces the peak mass loss rate of SAN40 at fire-level heat fluxes. The possible mechanism includes the following two primary aspects. One is the increased catalytic activity of the combination of Cloisite 20A and NHPMo probably due to the overlapping degradation temperature range of the combination of 20A/NHPMo and SAN40, which probably enhances char formation; the other is more NHPMo around or on the clay stacks and less in the galleries, which probably bridges these clay stacks with char formed around clay and form a stronger network during the degradation process. The resulting coherent residue, without cracks, on the heated polymer sample surface can slow inward heat transfer, suppress vigorous bubbling and hinder degradation products from escaping from the sample into the gas phase. Network structures are also formed in the SAN40/20A/NaPMo, SAN40/20A/ZnPMo and SAN40/20A/MEPMo composites, but they break down at higher temperatures. As a result, bubbling and cracking cannot be suppressed as effectively. Therefore, similar synergistic enhancements were not obtained between Cloisite 20A and NaPMo, ZnPMo or MEPMo.

Acknowledgment

M.F.L. acknowledges funding partially from the China State Scholarship and partially from the National Institute of Standards and Technology (NIST). X.Z. acknowledges the support of the MarylandNanoCenter and its NispLab. The NispLab is supported in part by the NSF as an MRSEC Shared Experimental Facility. T. K. acknowledges funding from the NIST under Grant 9H9184. We gratefully acknowledge Dr. Tom Ohlemiller at the NIST for helping with grammatical corrections.

References

- [1] Gilman JW, Jackson CL, Morgan AB, Harris R, Manias E, Giannelis EP, et al. *Chemistry of Materials* 2000;12:1866–73.
- [2] Kashiwagi T, Harris RH, Zhang X, Briber RM, Cipriano BH, Raghavan SR, et al. *Polymer* 2004;45:881–91.
- [3] Bourbigot S, Vanderhart DL, Gilman JW, Bellayer S, Stretz H, Paul DR. *Polymer* 2004;45:7627–38.
- [4] Stretz HA, Wootan MW, Cassidy PE, Ko JH. *Polymers for Advanced Technologies* 2005;16:239–48.
- [5] Shi Y, Kashiwagi T, Walters RN, Gilman JW, Lyon RE, Sogah DY. *Polymer* 2009;50:3478–87.
- [6] Wang Z, Du XH, Yu HO, Jiang ZW, Liu J, Tang T. *Polymer* 2009;50:5794–802.
- [7] Morgan AB. *Polymers for Advanced Technologies* 2006;17:206–17.
- [8] Levchik SV, Wei ED. *Polymer International* 2008;57:431–48.
- [9] Ribeiro SPS, Esteveao LRM, Pereira C, Rodrigues J, Nascimento RSV. *Polymer Degradation and Stability* 2009;94:421–31.
- [10] Chen XS, Yu ZZ, Liu W, Zhang S. *Polymer Degradation and Stability* 2009;94:1520–5.
- [11] Bourbigot S, Gilman JW, Wilkie CA. *Polymer Degradation and Stability* 2004;84:483–92.
- [12] Brauman SK. *Journal of Fire Retardant Chemistry* 1980;7:154–60.
- [13] Wang ZT, Jiang DD, Wilkie CA, Gilman JW. *Polymer Degradation and Stability* 1999;66:373–8.
- [14] Jang J, Kim J, Bae JY. *Polymer Degradation and Stability* 2005;88:324–32.
- [15] Jang J, Kim J, Bae JY. *Polymer Degradation and Stability* 2005;90:508–14.
- [16] Nawani P, Desai P, Lundwall M, Gelfer MY, Hsiao BS, Rafailovich M, et al. *Polymer* 2007;48:827–40.
- [17] Cai YB, Hu Y, Song L, Xuan SY, Zhang Y, Chen ZY, et al. *Polymer Degradation and Stability* 2007;92:490–6.
- [18] Yu H, Liu J, Wang Z, Jiang ZW, Tang T. *Journal of Physical Chemistry C* 2009;113:13092–7.
- [19] Kashiwagi T, Danyus R, Liu M, Zammarano M, Shields JR. *Polymer Degradation and Stability* 2009;94:2028–35.
- [20] Mizuno N, Misono M. *Chemical Reviews* 1998;98:199–217.
- [21] Kozhevnikov IV. *Chemical Reviews* 1998;98:171–98.
- [22] Kim YS, Wang F, Hickner M, Zawodzinski TA, McGrath JE. *Journal of Membrane Science* 2003;212:263–82.
- [23] Yadav GD, Kirthivasan N. *Journal of the Chemical Society-Chemical Communications*; 1995:203–4.
- [24] Yadav GD. *Catalysis Surveys from Asia* 2005;9:117–37.
- [25] Lee J, Kim H, La KW, Park DR, Jung JC, Lee SH, et al. *Catalysis Letters* 2008;123:90–5.
- [26] Wu Q, Qu BJ. *Polymer Degradation and Stability* 2001;74:255–61.
- [27] Johnson K, Viswanathan B, Varadarajan TK. *Reaction Kinetics and Catalysis Letters* 1998;63:365–70.
- [28] Li J, Wang XH, Zhu WM, Cao FH. *ChemSusChem* 2009;2:177–83.
- [29] Austin PJ, Buch RR, Kashiwagi T. *Fire and Materials* 1998;22:221–37.
- [30] Ilhan S, Kahruman C, Yusufoglu I. *Journal of Analytical and Applied Pyrolysis* 2007;78:363–70.
- [31] Jang BN, Wilkie CA. *Polymer* 2005;46:9702–13.
- [32] Y.X. Zhang, Y.Liu, Q.Wang, *Journal of Applied Polymer Science*. 116 45–49.
- [33] Kashiwagi T, Mu MF, Winey K, Cipriano B, Raghavan SR, Pack S, et al. *Polymer* 2008;49:4358–68.
- [34] Kashiwagi T. *Symposium (International) on Combustion* 1994;25:1423–37.
- [35] Gilman JW, Harris RH, Shields JR, Kashiwagi T, Morgan AB. *Polymers for Advanced Technologies* 2006;17:263–71.

Effect of heat treatment on the morphology and properties of poly(styrene-co-acrylonitrile)/montmorillonite nanocomposites

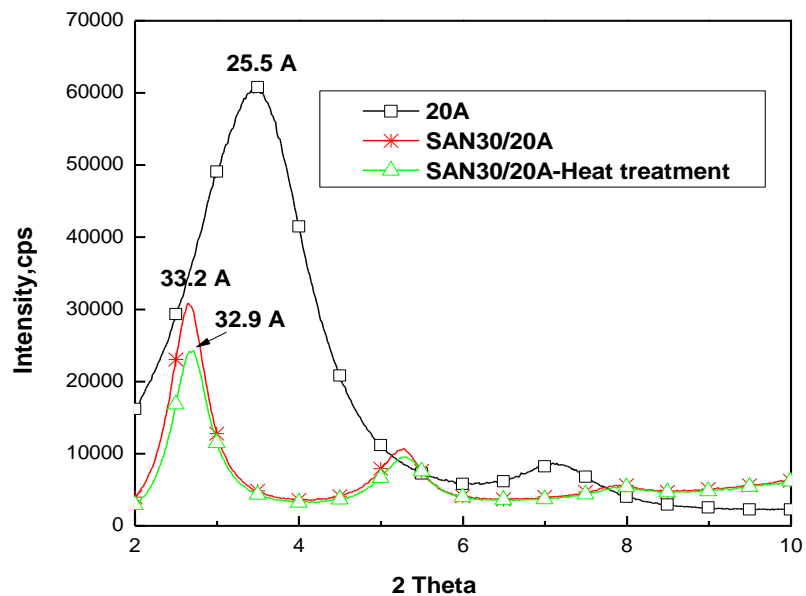
Introduction

Over the past two decades, there has been a significantly increasing interest in montmorillonite (MMT) due to their superior properties over conventional microcomposites. It is well established that the addition of relatively small amount of clay to polymers reduces flammability properties of the polymer. However, when polymer/clay nanocomposites are prepared, they may not be in the equilibrium state and clay particles might be slowly transported toward an equilibrium state. If this is the case, the clay dispersion level in a polymer tends to change and might reduce flame retardant effectiveness of polymer/clay nanocomposites. In order to hasten the transport rate of clay particles in a polymer, polymer/clay nanocomposites are heated at 80 °C for the duration of 72 hours. In this study, two types of organoclay (Cloisite 20A and Cloisites 30B) were used in poly(styrene-co-acrylonitrile). The morphology and flammability properties of SAN/MMT nanocomposites before and after the heat treatment have been measured. The possible mechanism of the influence of heat treatment on the flammability properties of SAN/MMT nanocomposites was also discussed.

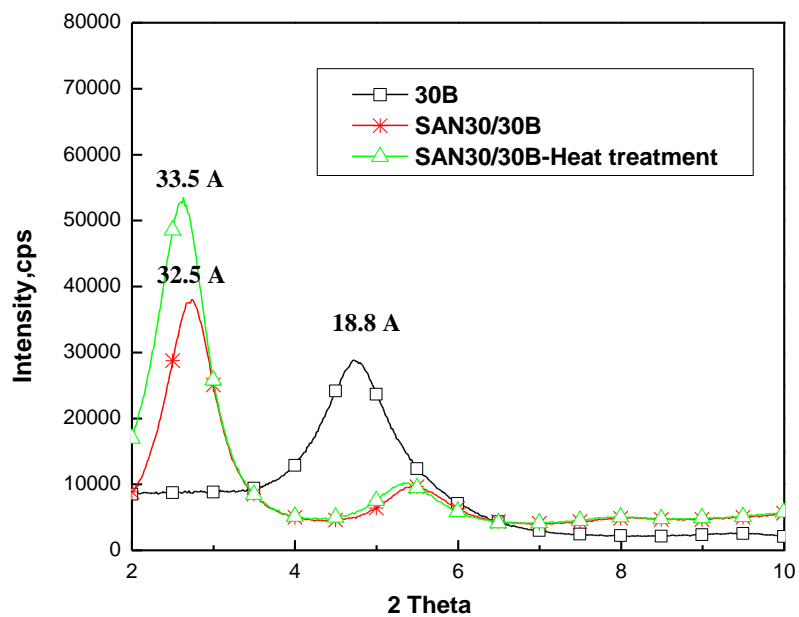
Results and discussion

1. Structure and morphology of SAN30 composites

The effect of heat treatment on structure and morphology of SAN30 composites were investigated by XRD, TEM and LSCM. As shown in Fig. 1, the peaks of SAN30/clay composites shift to lower 2θ values and the d_{001} spacing has increased with either Cloisite 20A or Cloisite 30B, indicating that the SAN30 chains have entered into the clay galleries, forming an intercalated structure. After the heat treatment, the peaks of SAN30/Cloisite 20A composites slightly shift to slightly lower 2θ values while those of SAN30/Cloisite 30B composites slightly shift to higher 2θ values. The heat treatment do not show any significant effect on the d_{001} spacing of SAN30/Cloisite 20A composites, but the d_{001} spacing of SAN30/Cloisite 30B composites increases from 32.5 Å to 33.5 Å.



(a)



(b)

Figure 1. XRD curves: (a) SAN30/Cloisite 20A(95/5) and (b) SAN30/Cloisite 30B(95/5).

The TEM images of SAN30/Clay composites are shown in Fig. 2. Clay stacks composed of a few layers and single clay platelets can be observed in both SAN30/Cloisite 20A composites and SAN30/Cloisite 30B composites, indicating that some extent of clay exfoliations has occurred. After the heat treatment, the TEM images show no significant changes.

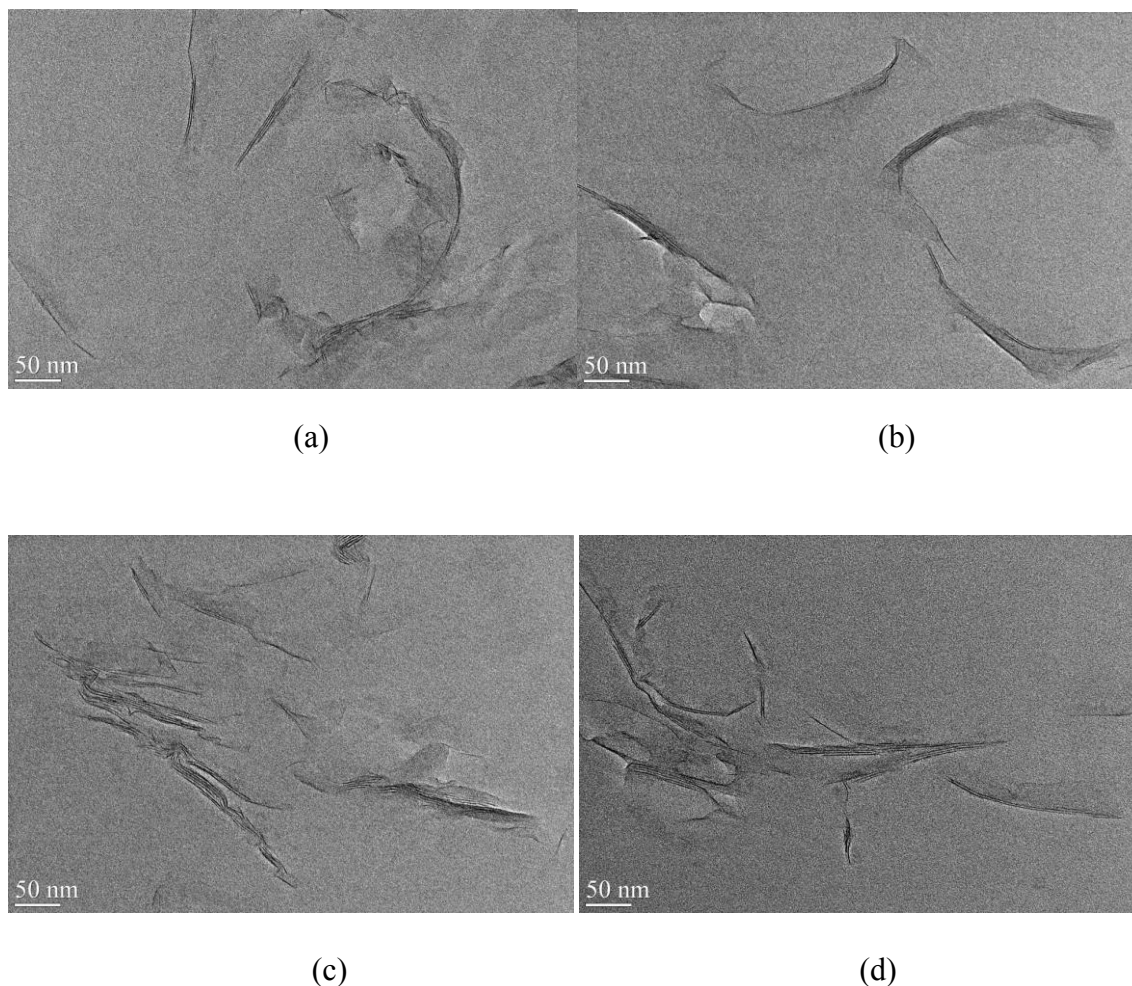
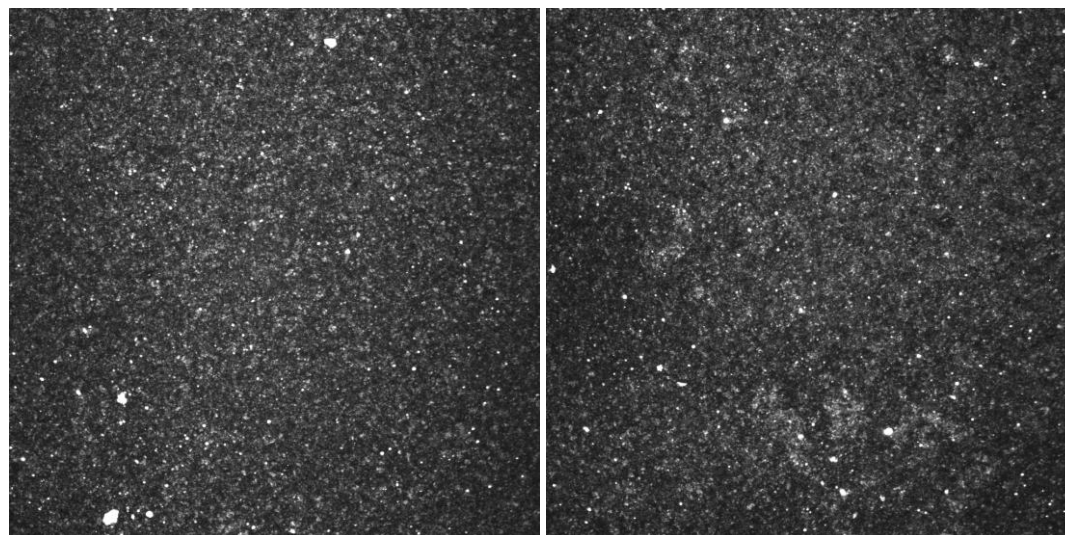


Figure 2. TEM images: (a) SAN30/Cloisite 20A(95/5), (b) SAN30/Cloisite 20A(95/5) after the heat treatment, (c) SAN30/Cloisite 30B(95/5), and SAN30/Cloisite 30B(95/5) after the heat treatment.

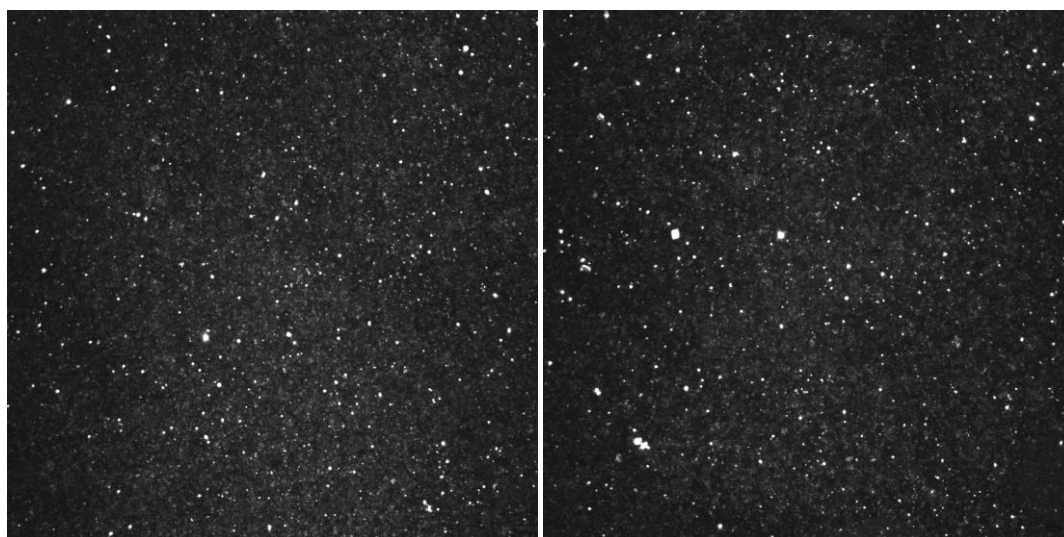
The 2D laser scanned confocal microscopy images of SAN30/Clay composites are shown in Fig. 3. Whether the clay is Cloisite 20A or Cloisite 30B, clay disperses well in SAN30 composites except having some small clay agglomerates. After the heat treatment, number of small clay agglomerates increases. Fig. 4 shows the relationship between the intensity and the frequency of pixels in the 2D projection pictures. Since the index of refraction of Cloisite 20A is less than that of Cloisite 30B ($n_{20A} = 1.4284$, $n_{30B} = 1.447$), the intensity of

SAN30/Cloisite 20A composites is stronger and the images are brighter. After heat treatment, the curves of both SAN30/Cloisite 20A-heat treatment and SAN30/30B-heat treatment shift to low intensity, indicating the dispersion level of clay decrease.



(a)

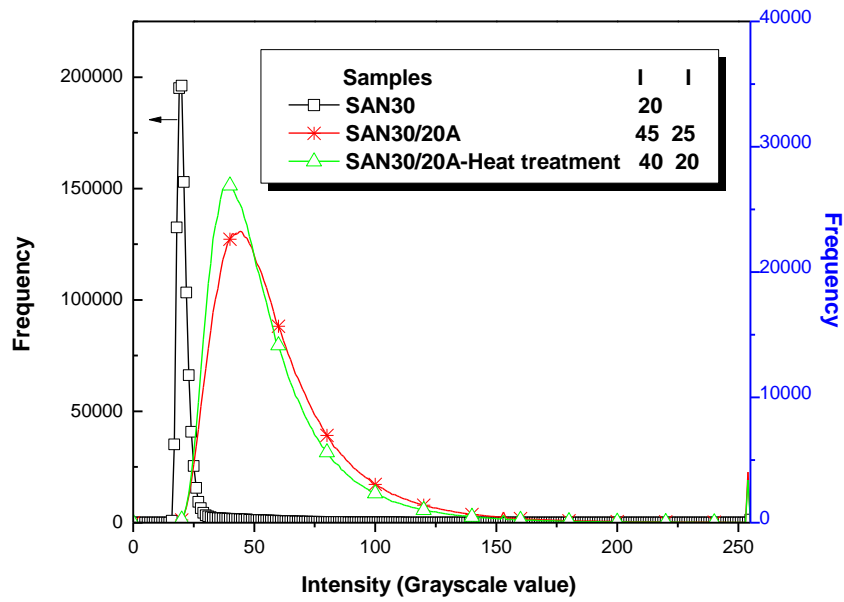
(b)



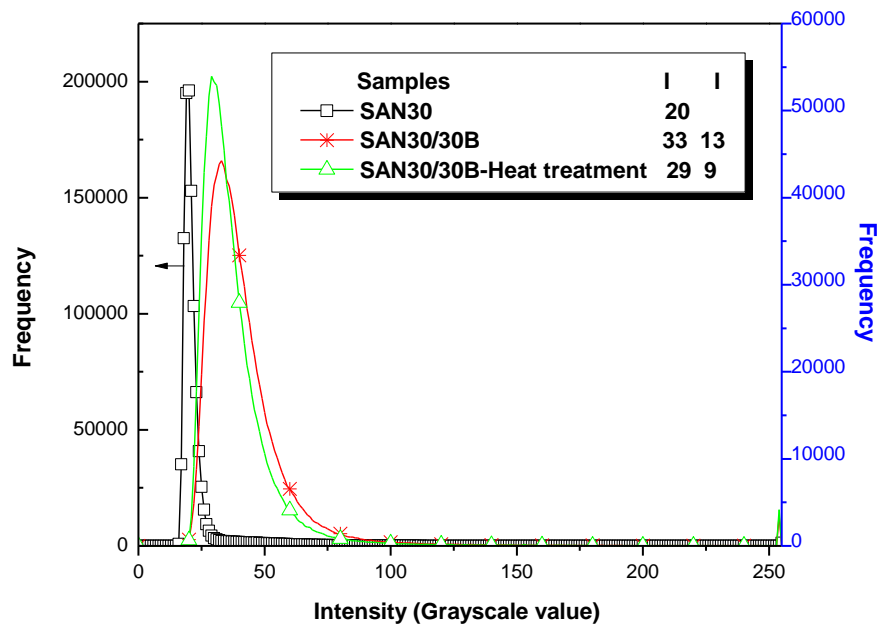
(c)

(d)

Figure 3. 2D confocal images: (a) SAN30/Cloisite 20A(95/5), (b) SAN30/Cloisite 20A(95/5) after the heat treatment, (c) San30/Cloisite 30B, and (d) SAN30/Cloisite 30B(95/5) after the heat treatment.



(a)



(b)

Figure 4. Clay spatial distribution expressed by the relationship between intensity and frequency in the confocal image analyses: (a) SAN30 and SAN30/Cloisite 20A(95/5), and (b) SAN30 and SAN30/Cloisite 30B(95/5).

the heat treatment, but TEM results show that clay stacks become more orderly and spatial

dispersion of clay becomes slightly worse. For SAN30/Cloisite 30B(95/5) composites, the heat treatment made little change in its morphology, probably due to the better miscibility between SAN30 and Cloisite 30B.

2. Properties

2.1. Thermal stability

The effect of heat treatment on thermal properties was measured by TGA. As shown in Fig.5, the TGA curves of SAN30 and SAN30/Cloisite 20A (95/5) composites are all close to each other below 400 °C. Both clay type and heat treatment show no significant effects on the thermal stability of SAN30.

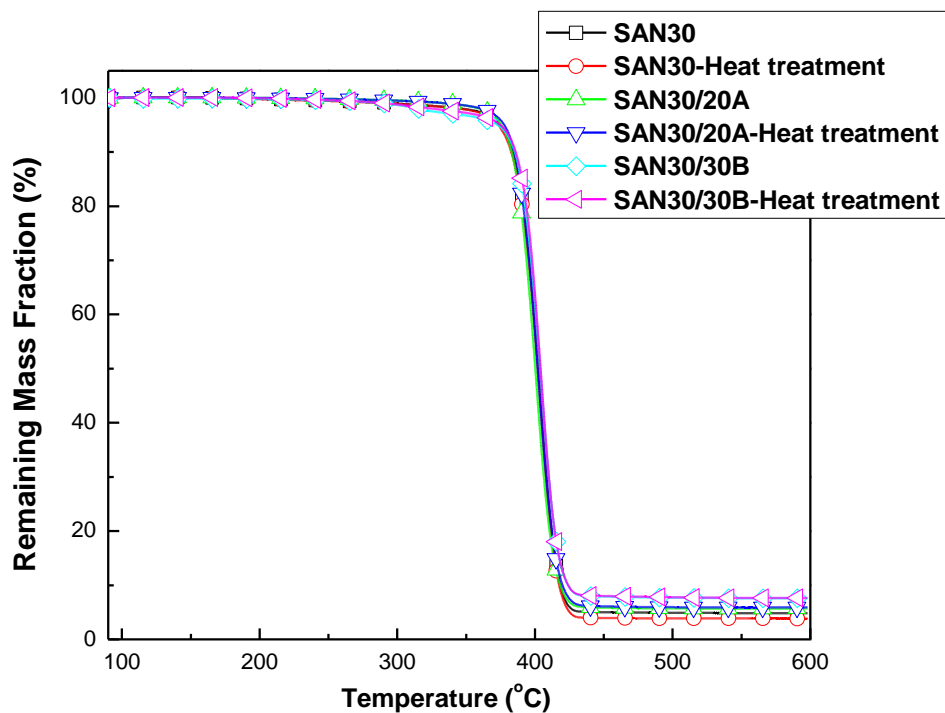


Figure 5. TGA curves of SAN30 and SAN30 composites at 5 °C/min in nitrogen.

2.2. Rheology

Figure 6 shows the temperature ramp of SAN30 and SAN30/Cloisite 20A(95/5) composites. Before heat treatment, the storage modulus of SAN30/Cloisite 20A(95/5) composites and SAN30/Cloisite 30B(95/5) composites are much higher than that of pure SAN30 at a fixed temperature. Compared with samples without heat treatment, the storage modulus of SAN30-heat treatment is slightly reduced above 230 °C while the storage modulus of SAN30/Cloisite 30B(95/5)-heat treatment composites is almost the same as that of SAN30/Cloisite 30B(95/5) at a fixed temperature, showing no significant effect of heat treatment on the rheological properties of SAN30 and SAN30/Cloisite 30B(95/5) composites. However, the storage modulus of SAN30/Cloisite 20A(95/5)-heat treatment composites is much reduced compared with that of SAN30/Cloisite 20A(95/5) composites.

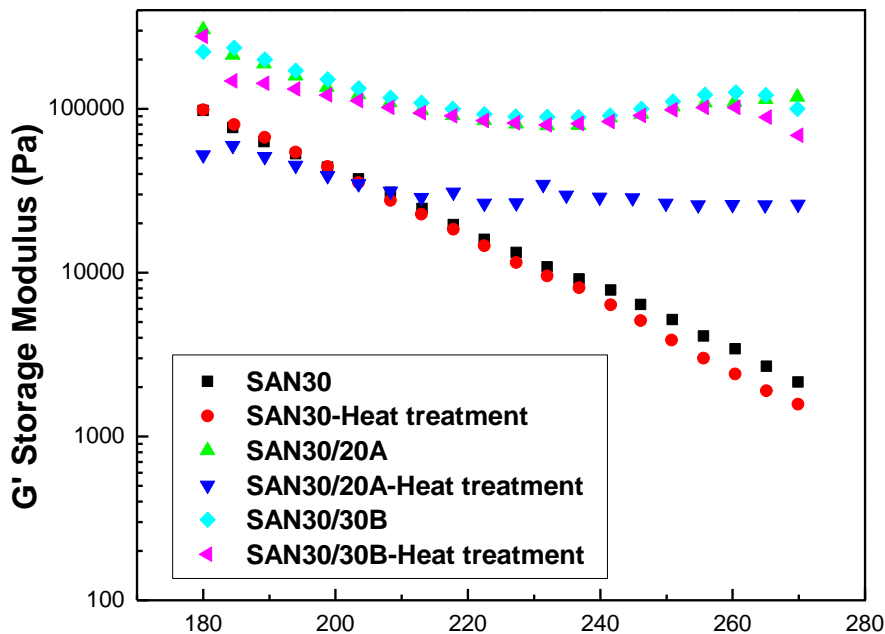


Figure 6. Temperature sweep of storage modulus of SAN30 and SAN30/Cloisite 20A(95/5) composites.

2.3. Flammability

The mass loss rate curves of SAN30 and the SAN30 composites at an external radiant flux of 50 Kw/m² in a nitrogen atmosphere are shown in Fig. 7. The mass loss rate of SAN30-heat treatment curves is almost the same as that of SAN30 except a little higher peak mass loss rate.

With the addition of either Cloisite 20A or Cloisite 30B, the peak mass loss rate is significantly reduced from that of SAN30. After the heat treatment, the mass loss rate curve of SAN30/Cloisite 20A(95/5) composites is higher than that of unheated SAN30/Cloisite 20A(95/5). However, the peak mass loss rate of SAN30/Cloisite 30B(95/5)-heat treatment is almost the same as that of SAN30/Cloisite 30B(95/5) composites while the peak mass loss rate of SAN30/Cloisite 20A(95/5) –heat treatment increased about 24% by heat treatment.

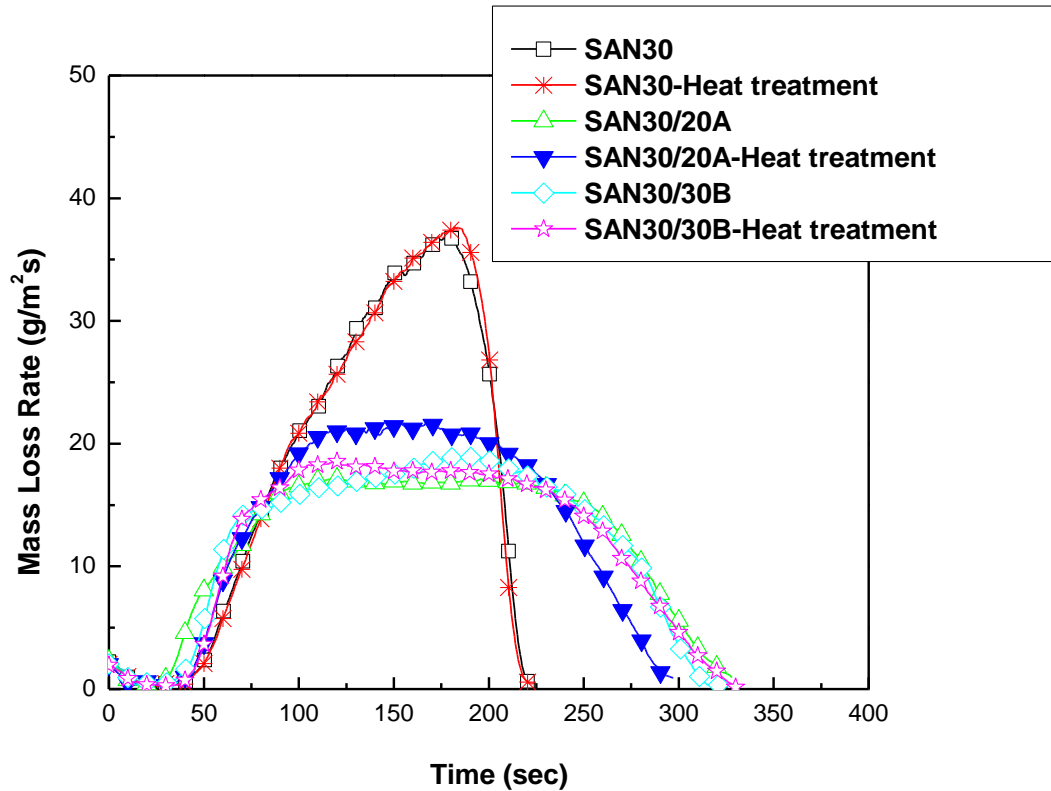


Figure 7. Mass loss rate curves of SAN30 and SAN30 composites at 50 kW/m² in nitrogen.

Conclusion

In this study, SAN30/Cloisite 20A(95/5) and SAN30/Cloisite 30B(95/5) nanocomposites were prepared by the solvent coagulation method. The structure, thermal stability, rheological properties and flammability properties of SAN30/Cloisite 20A (95/5) and SAN30/Cloisite 30B(95/5) nanocomposites before and after the heat treatment were investigated. The clay dispersion in SAN30/Cloisite 20A(95/5) and SAN30/Cloisite 30B(95/5) nanocomposites slightly becomes worse after the heat treatment. The thermal stability of SAN30/Cloisite 20A(95/5) and SAN30/Cloisite 30B(95/5) nanocomposites measured by TGA is not affected by the heat treatment, but the storage modulus of SAN30/Cloisite 20A(95/5)-heat treatment nanocomposites is reduced and its peak mass loss rate increases. However, little heat treatment effects are observed for SAN30/Cloisite 30B(95/5).